AGU PUBLICATIONS

Geochemistry, Geophysics, Geosystems

RESEARCH ARTICLE
10.1002/2016GC006507

Key Points:
- Isotropic tomography images of subduction zones are likely contaminated by artifacts
- This problem is not solved by increasing the azimuth and incidence angle diversity of the ray coverage
- Prescribing an approximate anisotropy field as an a priori constraint may be a useful approach

Supporting Information:
- Supporting Information S1

Correspondence to:
M. Bezada,
mbezada@umn.edu

Citation:
Bezada, M. J., M. Faccenda, and D. R. Toomey (2016), Representing anisotropic subduction zones with isotropic velocity models: A characterization of the problem and some steps on a possible path forward, *Geochem. Geophys. Geosyst.*, *17*, 3164–3189, doi: 10.1002/2016GC006507.

Received 29 JUN 2016
Accepted 11 JUL 2016
Accepted article online 14 JUL 2016
Published online 10 AUG 2016

Representing anisotropic subduction zones with isotropic velocity models: A characterization of the problem and some steps on a possible path forward

M. J. Bezada[1], M. Faccenda[2], and D. R. Toomey[3]

[1]Department of Earth Sciences, University of Minnesota-Twin Cities, Minneapolis, Minnesota, USA, [2]Department of Geosciences, Universitá di Padova, Padova, Italy, [3]Department of Geological Sciences, University of Oregon, Eugene, Oregon, USA

Abstract Despite the widely known fact that mantle flow in and around subduction zones produces the development of considerable seismic anisotropy, most P-wave tomography efforts still rely on the assumption of isotropy. In this study, we explore the potential effects of erroneous assumption on tomographic images and explore an alternative approach. We conduct a series of synthetic tomography tests based on a geodynamic simulation of subduction and rollback. The simulation results provide a self-consistent distribution of isotropic (thermal) anomalies and seismic anisotropy which we use to calculate synthetic delay times for a number of realistic and hypothetical event distributions. We find that anisotropy-induced artifacts are abundant and significant for teleseismic, local and mixed event distributions. The occurrence of artifacts is not reduced, and indeed can be exacerbated, by increasing richness in ray-path azimuths and incidence angles. The artifacts that we observe are, in all cases, important enough to significantly impact the interpretation of the images. We test an approach based on prescribing the anisotropy field as an a priori constraint and find that even coarse approximations to the true anisotropy field produce useful results. Using approximate anisotropy, fields can result in reduced RMS misfit to the travel time delays and reduced abundance and severity of imaging artifacts. We propose that the use of anisotropy fields derived from geodynamic modeling and constrained by seismic observables may constitute a viable alternative to isotropic tomography that does not require the inversion for anisotropy parameters in each node of the model.

1. Introduction

Subduction systems are a major source of magmatism on Earth, second only to mid-ocean ridges. The processes that result in arc and back-arc volcanism: flux melting, decompression melting, and slab melting, as well as the migration and accumulation of this melt, are among the most important processes in the earth sciences. A thorough characterization of these systems is needed to understand not only subduction-related volcanism, but also the cycling of water and other volatiles between the lithosphere and the convecting mantle. Because of the well-known sensitivity of seismic velocities to temperature, melt fraction, and volatile content, seismic tomography can image each of these as velocity anomalies; providing a powerful tool for investigating the current day configuration of subduction zones as it relates to these thermo-petrological processes.

In the last two decades, the increased availability of seismic data from dense seismometer deployments has enabled the production of tomography models with ever-increasing resolution. As a result, velocity anomalies with spatial length scales of 100 km or less now appear to be robustly imaged. The increased resolution justifies the interpretation of smaller scale features, and of the detailed geometry of larger features such as subducted slabs. While determining the geometry of mantle velocity anomalies has been historically the major contribution of seismic tomography, it is now common to use the magnitude of the imaged anomalies to go a step further. Recent experimental and theoretical work in petrology and mineral physics has provided a better understanding of the dependence of seismic velocities on different physical parameters [e.g., *Mainprice*, 1997; *Karato and Jung*, 1998; *Hammond and Humphreys*, 2000; *Takei*, 2002; *Cammarano et al.*, 2003; *Jackson and Faul*, 2010]. As a result, while many challenges remain, a quantitative estimate of the physical state of the mantle can potentially be extracted from seismic images. Seismic velocity structure

derived from tomography has been interpreted in terms of temperature and melt fraction in subduction zones [e.g., *Wiens et al*., 2008], individual arc volcanoes [e.g., *Paulatto et al*., 2012], mid-ocean ridges [e.g., *Toomey et al*., 1998; *Hammond and Toomey*, 2003], mantle plumes [e.g., *Bijwaard and Spakman*, 1999; *Wolfe et al*., 2009; *Villagómez et al*., 2014], and continental regions at various scales [*Sobolev et al*., 1997; *Goes et al*., 2000; *Goes and van der Lee*, 2002]. Furthermore, seismically derived temperature models can be used to infer density and drive mantle flow simulations [*Faccenna and Becker*, 2010].

As we rely more heavily on tomographic images for interpretations, and as we use them to generate a wider array of derived products, it becomes increasingly important for the models to be accurate representations of the subsurface beyond the first-order geometry of the major features. This is only possible if the models account for all first-order observations, including seismic anisotropy. Anisotropy in the mantle is a well-understood phenomenon that is caused by the alignment of crystals of intrinsically anisotropic minerals (primarily olivine) as a response to mantle flow (crystallographic-preferred or lattice-preferred orientation, CPO or LPO) or from the alignment of materials with different bulk properties such as melt-filled cracks (shape-preferred orientation). The development of LPO anisotropic fabric in mantle minerals is well documented in laboratory experiments [e.g., *Karato et al*., 2008]. Therefore, mantle seismic anisotropy is a good indicator of recent deformation and flow patterns. Especially in the last two decades, the study of anisotropy from observations of shear-wave splitting has provided much insight into mantle flow patterns in subduction zone settings. Regional studies, as well as global compilations, show that mantle flow in subduction zones is often complex and three-dimensional, and that it produces substantial anisotropy in the arc and back-arc regions, as well as the subslab mantle [e.g., *Russo and Silver*, 1994; *Long and Silver*, 2008, 2009; *Long*, 2013; *Olive et al*., 2014].

Despite the noncontroversial nature of seismic anisotropy in and around subduction zones, teleseismic body-wave tomography largely remains isotropic. While surface wave tomography that includes radial anisotropy is becoming common, this scenario has the advantage of being essentially a 2-D problem. Bringing anisotropy into the volumetric problem of body-wave tomography on regional scales poses a significant challenge, since trying to invert for the direction and magnitude of anisotropy would potentially quadruple the number of parameters in what is already an underdetermined problem. For this reason, with few exceptions [e.g., *Hammond and Toomey*, 2003; *Eberhart-Phillips and Henderson*, 2004; *Ishise and Oda*, 2005; *Koulakov et al*., 2009; *Tian and Zhao*, 2012; *Wang and Zhao*, 2013; *Huang et al*., 2015], the assumption of isotropy is still prevalent in body-wave tomographic imaging.

Given that incidence angles of teleseismic arrivals are overwhelmingly steep, teleseismic waves mostly propagate in a direction subparallel to the anisotropic slow direction in those regions where the horizontal flow-derived anisotropy in the mantle aligns the seismically fast-axis of olivine in the horizontal plane. Consequently, horizontal flow-induced anisotropy would produce delays similar to those caused by isotropic slow anomalies. In a tomography model, artificial velocity perturbations resulting from an inadequate accounting for anisotropy would thus interfere with real velocity anomalies caused by partial melt, hydration, and excess temperature. The confounding effect of the expected artifacts potentially hinders accurate quantitative interpretations of velocity models in terms of physical (thermopetrological) parameters. Subvertical flow is also present as entrained mantle descends along with the subducting slab. Upgoing teleseismic arrivals may travel at small or large angles to the fast direction of anisotropy depending on their backazimuth, creating complicated delay patterns that may result in distortions to the slab geometry as imaged by tomography. In this paper, we take advantage of recent advances in micro-macro geodynamic modeling to gain insight into the possible location, extent, and magnitude of anisotropy-produced artifacts in P-wave tomography imaging of subduction zones. Our goals are to understand how these artificial anomalies may affect interpretation of the tomographic images in terms of physical processes, and to explore ways in which we can remove or reduce their prevalence in the model. Regarding the latter, we begin to explore a novel approach that sidesteps the issues that can arise when attempting inversion for anisotropy parameters on a 3-D volume.

Previous efforts to address the effect of neglected anisotropy have almost unanimously found that it can produce significant teleseismic time delays that, under certain conditions, could substantially bias P-wave tomography results [*Kendall*, 1994; *Blackman et al*., 1996; *Grésillaud and Cara*, 1996; *Blackman and Kendall*, 1997; *Sobolev et al*., 1999; *Wu and Lees*, 1999; *Sieminski et al*., 2007; *Lloyd and van der Lee*, 2008]. Anisotropy effects are especially notable when the fast axes are dipping, such as in a subduction setting [*Sobolev et al*.,

1999; *Sieminski et al*., 2007] or at upwellings beneath mid-ocean ridges [*Toomey et al*., 1998; *Hammond and Toomey*, 2003], and are significant even when finite-frequency effects are taken into account [*Sieminski et al*., 2007]. For S-wave tomography, *Lloyd and van der Lee* [2008] concluded that any artifacts caused by anisotropy are likely to be small, but we note that their numerical experiments did not consider dipping fast axes or depth-dependent anisotropy and that the resolution of both the anisotropy field estimates and the tomography models in their study is low by current standards.

To carry out our numerical experiments, we use a state of the art method for modeling the development of anisotropic fabric in the mantle during subduction. Output of this modeling provides the isotropic (i.e., thermal) velocity variations as well as the anisotropy field for the model domain. With this information, we produce sets of synthetic travel-time delays that can be inverted assuming isotropy, as is common practice. Our approach is novel in that we investigate a synthetic volume where the estimates of the isotropic velocity anomalies and the anisotropy field are physically based, mutually consistent, and recreate a typical subduction scenario. The synthetic data we invert include the travel-time effects of both the target isotropic structure and the potentially contaminating seismic anisotropy, enabling us to compare the relative contribution of each to the result. Additionally, our numerical experiments are performed on spatial scales and with source-receiver geometries relevant to current and future regional-scale imaging of subduction zones.

Our results strongly suggest that isotropic subduction zone tomography can be contaminated by anisotropy-related artifacts. These artifacts may have large spatial length scales and magnitudes that would make them first-order features of an isotropic tomography model, and may substantially compromise interpretations. In the final sections, we show that progress can be made by utilizing insight into the possible distribution of anisotropy in the subsurface from splitting observations and modeling results.

2. The Geodynamic Model

The starting point of our numerical experiments is the geodynamic simulation of the evolution of a subduction zone. From this modeling, we obtain a hypothetical volume of mantle that can be interrogated seismically. For these experiments, we model a subduction zone that consists of a slab with a half-width of 700 km that subducts freely in response to its negative buoyancy and stagnates over the 660 km discontinuity. The method for petrological-thermomechanical modeling has been described extensively in *Faccenda* [2014]. Here, we will briefly mention that the development of anisotropic fabric is simulated by micromechanical modeling of the alignment of crystals within polymineralic aggregates which are passively advected through the model by the mantle flow field. The modal abundances of the aggregates reflect a pyrolitic mantle composition (Wd:Grt = 60:40 for the upper transition zone, 410–520 km; Rw:Grt = 60:40 for the lower transition zone, 520–660 km; Bridgmanite:MgO = 80:20 for the lower mantle, > 660 km), with the exception of the upper mantle where a more appropriate harzburgitic composition is chosen (Ol:Ens = 70:30, 30–410 km) [*Mainprice*, 2007; *Faccenda*, 2014]. At each time step, the anisotropic fabric for each polycrystalline aggregate is calculated using the method of *Kaminski et al*. [2004], modified to account for nonsteady state deformation and deformation history, which in subduction zones can be complex [*Faccenda and Capitanio*, 2012, 2013], and strain-induced LPO of midmantle aggregates. The micromechanical modeling yields the full elastic tensor for each aggregate scaled by the local P-T conditions calculated by the thermomechanical modeling [*Faccenda*, 2014]. Interpolating the elastic moduli from the Lagrangian aggregates throughout the model domain allows us to calculate the anisotropy and seismic velocities anywhere in the model with any direction of propagation and polarization.

The isotropic velocity structure of the model is extracted from the full elastic tensors (Figure 1). The only large-scale isotropic (thermal) anomaly corresponds to the subducted slab itself, which is 3–4% faster than the 1-D reference model above the 410 km discontinuity. Directly above and below the 410 km discontinuity, the slab becomes wider and the amplitudes reach 5%. Deeper than ~435 km the maximum anomaly amplitude decreases to ~2% owing to a lower temperature dependence of the minerals' elastic moduli, and the slab becomes thinner. The only anomalies additional to the slab itself are three small (100–120 km in diameter) high-velocity anomalies with amplitudes of ~2% located east of the slab within the transition zone. These small anomalies are caused by fragments of the subducted lithosphere that became detached from the main slab during the simulated descent into the mantle.

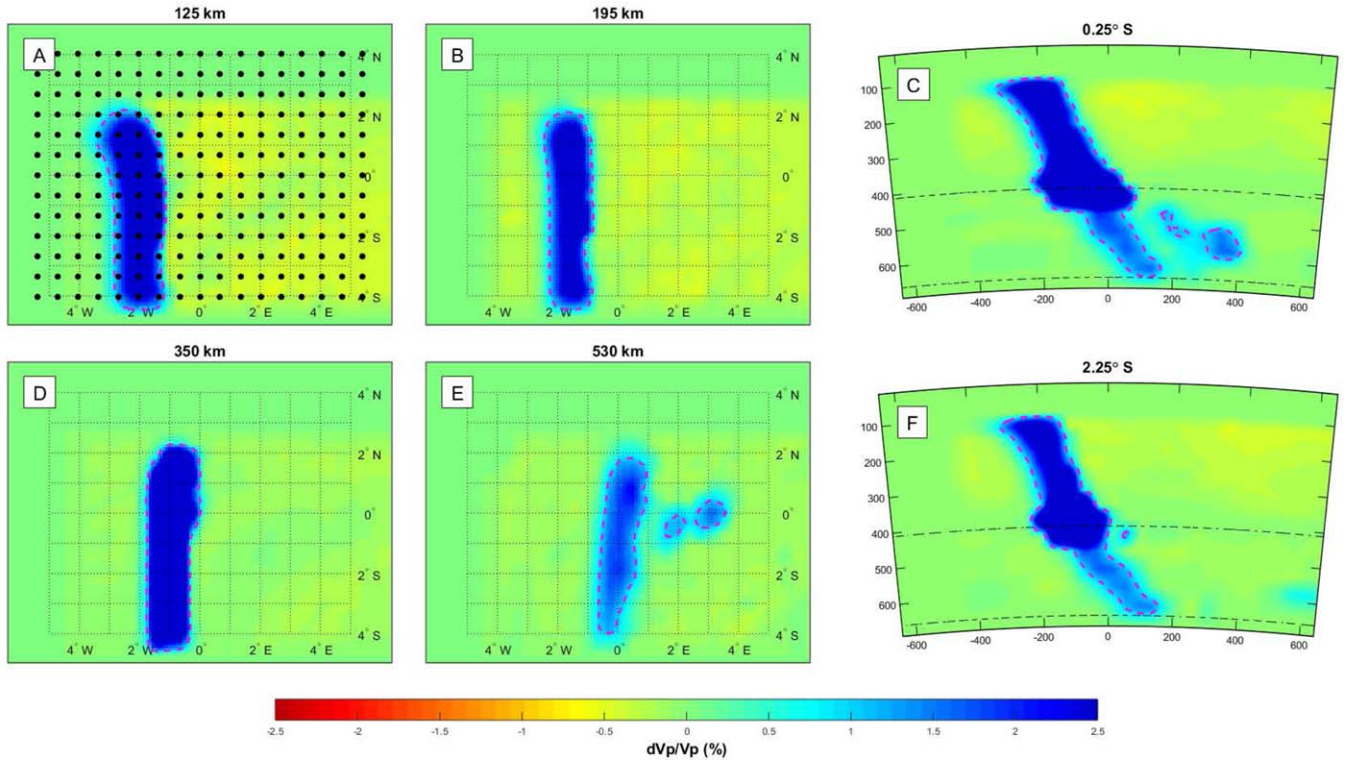

Figure 1. Isotropic velocity structure of "true" model. Four depth slices (a, b, d, e) and two East-West cross-sections (c–f) are shown at the depths and latitudes indicated in each plot. The isotropic velocity anomalies are derived from the result of thermomechanical modeling. "Isotropic" travel time delays were calculated by ray-tracing through this model. Magenta-colored dashed lines represent 1% fast isovelocity contours. These will be used as reference when comparing with inversion results.

The anisotropy that develops in the shallow upper mantle of the model is characterized by subhorizontal fast axes with trench-oblique to trench-perpendicular orientations in the arc and back-arc regions (Figure 2). Directly beneath the subducting slab, a ∼90 km thick layer of entrained mantle shows steeply dipping fast axes. Below the entrained layer, the subslab mantle is dominated by extension-induced, trench-parallel fast axes. This fabric is produced as the horizontally diverging mantle is evacuated in response to rollback. Steeply dipping fast axes also occur in the arc region within entrained mantle on the top side of the slab, and especially near the middle of the subducted slab where they are caused by subduction-induced poloidal flow in the mantle wedge. In general, anisotropy is significant above the transition zone and the magnitude of anisotropy decreases with depth, especially below 300 km (supporting information Figure S1). Between 100 and 300 km depth, the mean anisotropy percentage—defined as (Vpmax − Vpmin)/Vpavg * 100—is 2.5, and the maximum percentage is ∼7.

Although the model accounts for both diffusion and dislocation viscous creep, most of the deformation in the upper mantle is accommodated by dislocation, which may result in an overestimation of LPO development. As a check on the anisotropy values produced by the modeling procedure, we calculate synthetic SKS splitting observations using *fstrack* routines [*Becker et al*., 2006a] and obtain a distribution of splitting times with a peak at ∼1.2 s (supporting information Figures S2a and S2b).With the exception of a few very high (∼3 s) values, the distribution of the simulated splitting times is comparable to what is observed in real subduction settings that involve narrow slabs such as the Cascadia [*Liu et al*., 2014; *Bodmer et al*., 2015], Calabria [*Baccheschi et al*., 2007], and Alaboran slabs [*Diaz et al*., 2010; *Miller et al*., 2013] (supporting information Figures S2c–S2h), which suggests that the anisotropy developed in the model is a reasonable approximation to the real anisotropy distribution in complex subduction zones.

Figure 3 and supporting information Figures S3 and S4 show the apparent propagation velocities along different directions for P and S waves, as well as the apparent Vp/Vs ratios. Given the strong and laterally heterogeneous anisotropy, there are strong lateral variations of apparent velocity that affect Vp and Vs

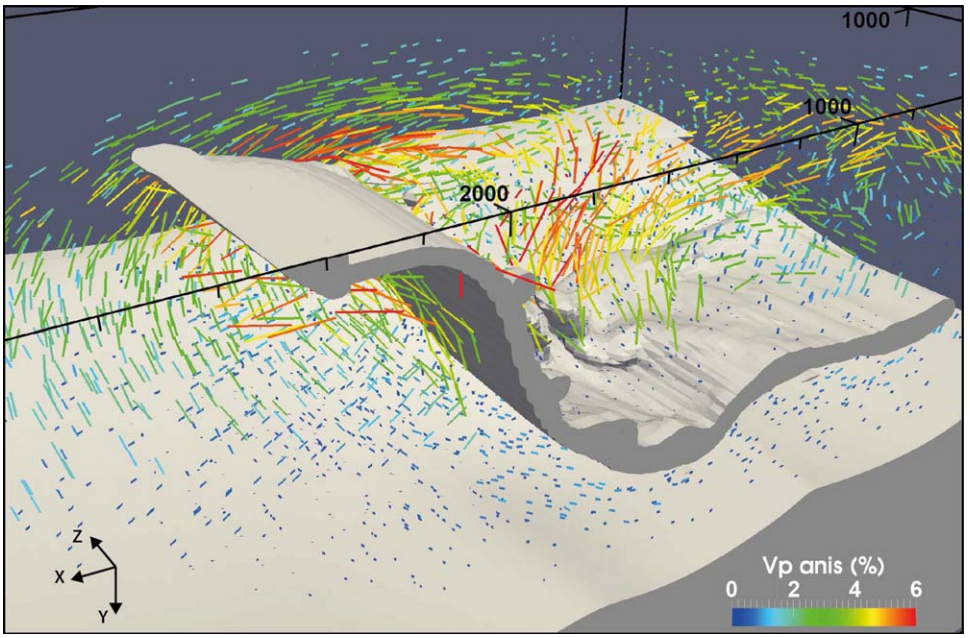

Figure 2. Vp anisotropy field for the "true" model. Light gray volumes represent areas of the model with viscosity above 9×10^{22} Pa·s with the subducted slab being clearly identifiable. Colored bars represent the anisotropy developed in the polycrystalline aggregates. Bar orientation indicates the fast Vp propagation direction, and bar length and color indicate magnitude of anisotropy.

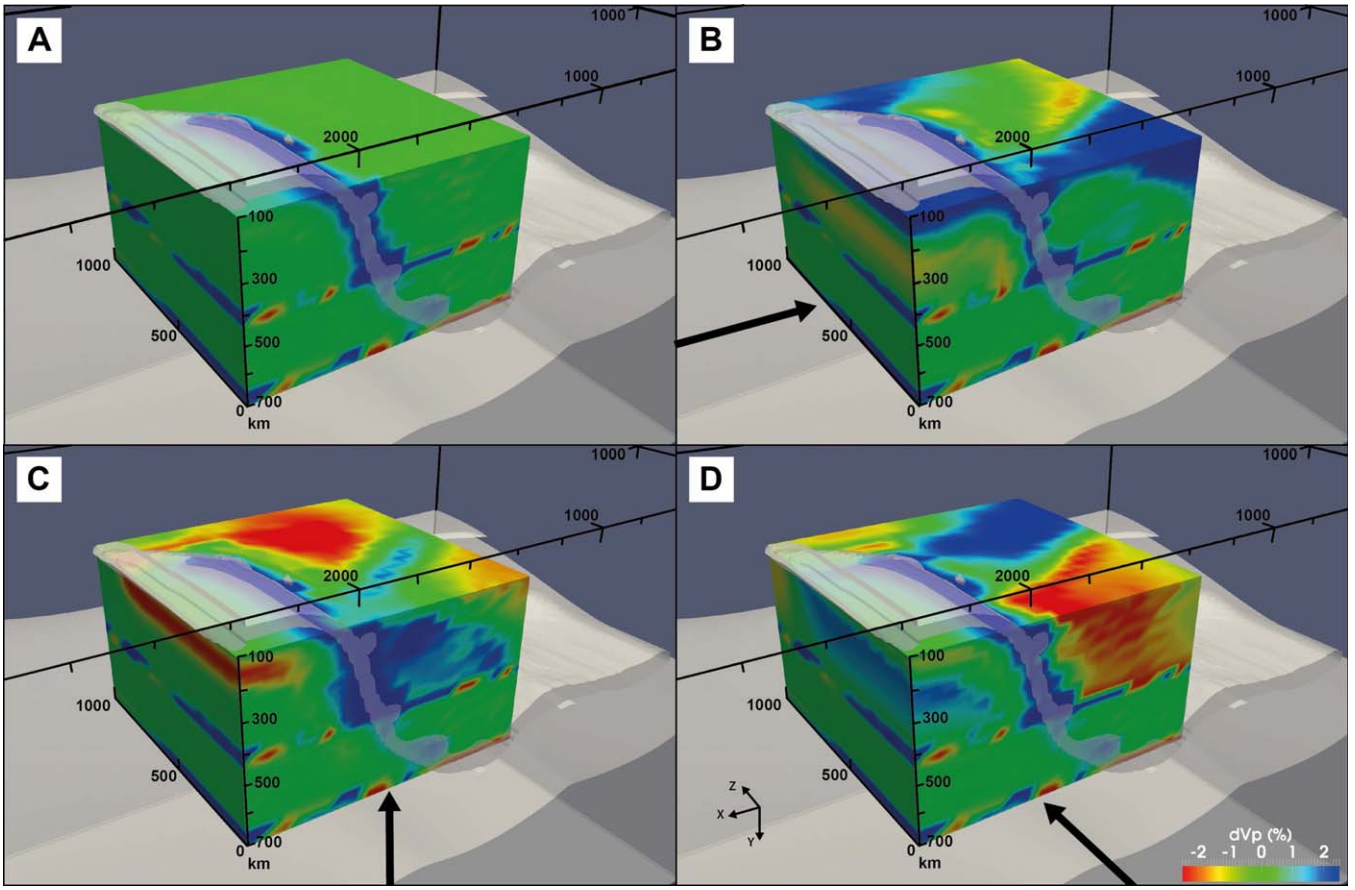

Figure 3. Isotropic and direction-dependent Vp anomalies for the "true" model. Views of dVp/Vp for the input model when considering isotropic velocities (a), and anisotropic velocities when the direction of propagation is East-West (b), vertical (c), and North-South (d). For clarity, the voxels corresponding to the slab are translucent. For similar figures showing dVs_1/Vs_1 and Vp/Vs_1 ratio, the reader is referred to the supporting information.

differently, and thus have significant effects of the apparent Vp/Vs ratio. In the following two sections we explore how these apparent, anisotropy-induced velocity variations could be mapped into isotropic anomalies by P-wave seismic tomography under several hypothetical event distribution scenarios.

3. Forward and Inverse Problems

For the purpose of conducting our synthetic tomography experiments, we define a smaller model domain that represents a region of interest within the original geodynamic model. This region has an area of 2000 by 1700 km^2 and a maximum depth of 700 km. We choose a coordinate system such that the slab trends in the north-south direction, and it dips toward the east.

The array of synthetic receivers is distributed over a grid with a constant station spacing of 75 km in both the north-south and east-west directions (Figure 1a). The resulting array covers an area of 1000 $\times$ 700 km^2 with 221 stations, which is comparable to large, dense, modern deployments. The center of the array is arbitrarily defined as 0°N and 0°E. While we use the same station locations for all our numerical experiments, we use a suite of event distributions to represent both realistic cases and hypothetical ones. We consider teleseismic as well as local (within the model domain) sources, and combinations of these, to assess the effect of raypath geometries on the imaging. The different event distributions will be described in detail in the following sections.

In order to generate synthetic delays from our station and event distributions, we use the hybrid ray tracing method of *Bezada et al*. [2013] (1-D velocity model outside the model domain, 3-D inside). Travel time calculations through the laterally heterogeneous, anisotropic velocity model use the infinite-frequency approximation (i.e., ray theory). The 3-D ray tracing procedure is based on graph theory [*Dijkstra*, 1959; *Moser*, 1991; *Toomey et al*., 1994] and is currently limited to anisotropy with a hexagonal symmetry. We therefore approximate the full elastic tensors retrieved from the geodynamic modeling to the best-fit hexagonal symmetry tensor using routines from D-REX [*Kaminski et al*., 2004]. By adopting the hexagonal symmetry approximation, we are intrinsically assuming that the orientation of the slow and intermediate axes of olivine is more random than that of the fast axis, and not capturing the full complexity of anisotropic propagation. Despite these limitations, it has been shown that the hexagonal component accounts for most of the anisotropy in the mantle [*Becker et al*., 2006b], making this a robust approximation for calculating the first-order effects we aim to study. The approximated anisotropy values are interpolated onto the ray-tracing grid which has a spacing of $\sim$10 km. This parameterization allows for high-fidelity representation of the isotropic structure and the anisotropy field. We do not add random noise to the synthetic delays, since our intention is to isolate the effect of the anisotropy.

The inverse problem is solved on a coarser grid where nodes are distributed in a plaid pattern. Node spacing beneath the array footprint is 42 km and increases to 56 km toward the edges of the model domain. Vertical node spacing increases with depth from 15 km for the first couple of layers to 35 km at 90 km depth and increasing in 5 km steps to 55 km at the bottom of the model The inversion method is that of *Bezada et al*. [2013] which is an iterative extension to 3-D ray tracing of the method of *Schmandt and Humphreys* [2010]. The inversion is regularized by imposing constraints on model norm and model roughness where the relative importance of these can be varied. The parameters that govern regularization were adjusted for each of the different event distributions in order to account for the different amounts of synthetic travel-time data. In this way, we assured that the relative weight of satisfying the regularization versus the data constraints was the same for all cases, resulting in an equivalent level of damping and smoothing. The models presented here are the result of three iterations of the algorithm, which is sufficient for the model to stabilize.

It is worth noting that since our forward calculations employ a ray-theoretical approach, they do not capture finite-frequency effects. However, for frequencies of $\sim$1 Hz, the width of the first Fresnel zone is small relative to the spacing of the inversion nodes and to the length scales of lateral variation of the isotropic structure and the anisotropy field. Under these conditions, ray-theory is a valid approximation. The use of 1 Hz data is common in regional tomography studies with length scales and resolution comparable to what we aim to simulate, especially for P-wave imaging. For these reasons, our approach is relevant for a large proportion of subduction imaging efforts.

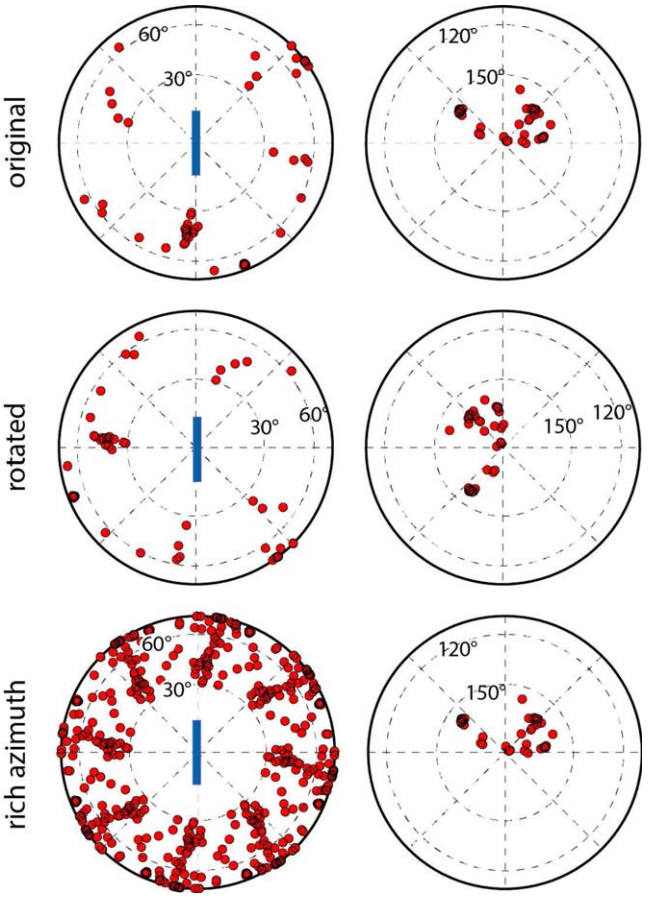

Figure 4. Teleseismic event distributions for the three cases considered. Each plot shows an orthographic projection centered on the center of the array footprint (left column) or the antipode of the array (right column). Dashed lines show equal epicentral distance and backazimuth. Epicentral distances of 30, 60, 120, and 150 are labeled on the plots. Red dots represent the events. The blue bars show the trench-parallel orientation for our model geometry.

4. Inversions, Teleseismic Cases

We consider three teleseismic cases all based on a template of event distribution taken (in terms of event epicentral distance and back-azimuth from the center of the array) from a study of the southeast Caribbean [*Levander et al.*, 2006; *Bezada et al.*, 2010]. This represents a realistic teleseismic event distribution, and corresponds to ~18 months of recording (a common duration for a temporary seismic deployment). The overrepresentation of certain azimuths is typical, given the uneven distribution of earthquakes in the earth, and is one of the factors that may affect imaging of anisotropic structure.

To explore the sensitivity of results to azimuthal coverage, we consider three different cases (Figure 4):

1. Original: the event distribution is exactly as for the experiment in the southeast Caribbean. A large fraction of the events have southerly azimuths that make them generally trench-parallel with respect to our synthetic subduction zone.
2. Rotated: the event azimuths are rotated by 90°. This event distribution has exactly the same heterogeneity in ray coverage as the original case and the position of the events relative to each other does not change. However, the azimuthal rotation means that in this case it is the trench-perpendicular azimuths that are relatively oversampled.
3. Rich azimuth: this represents a purely hypothetical distribution that is much more homogeneous in terms of azimuthal coverage than is possible on Earth. The purpose of this exercise is to gain insight by eliminating the issue of uneven ray distribution, thus isolating the problem of inverting anisotropic teleseismic delays while assuming isotropic structure. The distribution was created by taking the original distribution and, excluding antipodal events, adding copies of all the events rotated by 45–315° in 45° increments (Figure 4).

For each of these cases, we first calculate delays considering only the isotropic velocity structure to be used in reference inversions. A second set of delays that includes the effects of the anisotropy field is also calculated for each distribution.

For all three cases, we observe that the inversion of the isotropic delays is quite successful in reproducing the input isotropic velocity anomalies in terms of depth-extent and width, while amplitudes are only recovered at 60–70% of their true values (Figure 5 and supporting information Figures S5 and S6). Only minor differences distinguish the three models. In all of the models, the only significant anomaly is that which represents the subducted slab. As in the true model, this high-velocity anomaly appears continuous both laterally and in depth. Large artifacts are absent, with spurious low-velocity anomalies dotting the model, but none of the exceeding an amplitude of 0.5%; or less than a fifth of the amplitude of the slab anomaly. The small detached anomalies present in the transition zone in the input model are detected in the

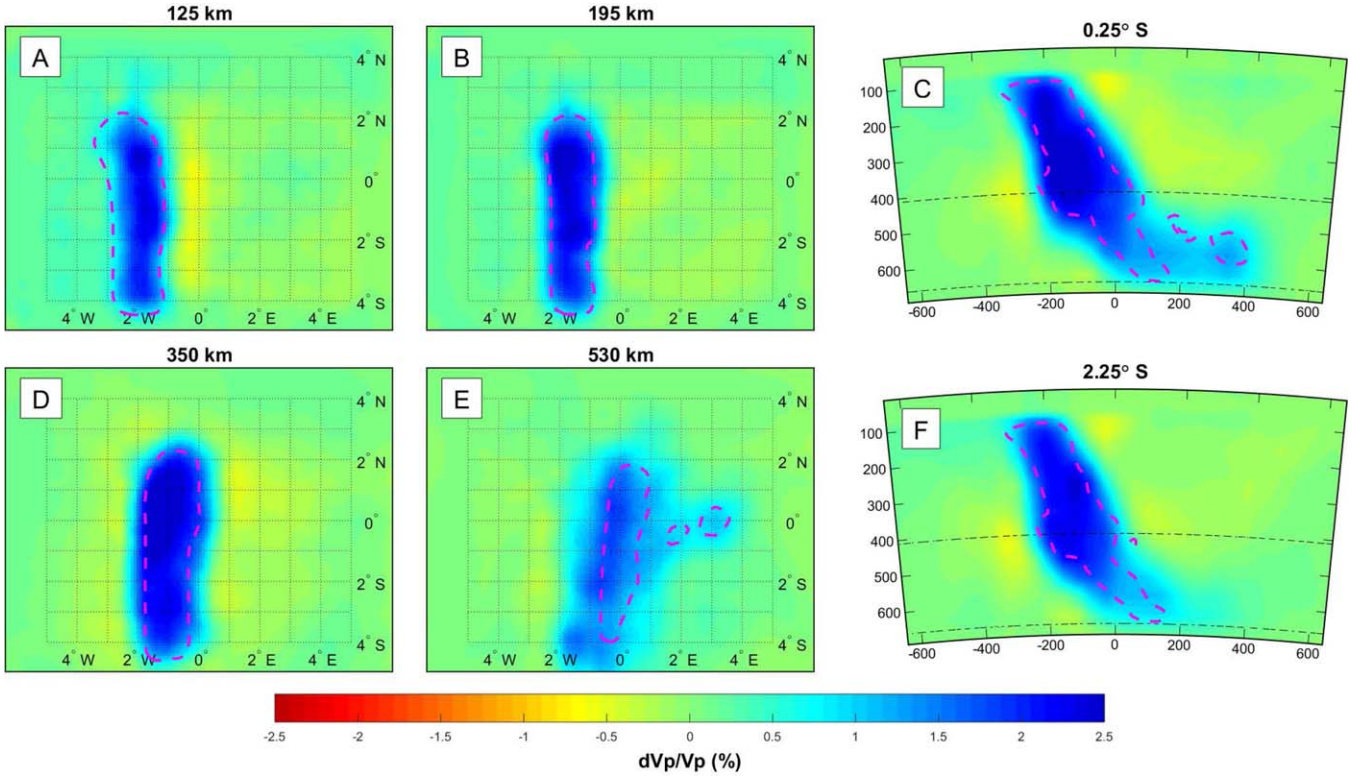

Figure 5. Results of inverting isotropic delays for the "original" teleseismic event distribution. Input travel-time delays were derived from the model of Figure 1, without taking into account anisotropy. Four depth slices (a, b, d, e) and two East-West cross-sections (c, f) are shown at the depths and latitudes indicated in each plot. Depth slices and cross sections correspond to those shown in Figure 1, and the 1% isovelocity contours for the "true" model are shown as magenta-colored dashed lines for reference. When inverting isotropic delay times, large artifacts are absent. For similar figures showing the results of isotropic inversion using the other two teleseismic event distributions (rotated and rich azimuth, Figure 4), the reader is referred to the supporting information.

inversions although they are not resolved as separate from the main body of the slab (Figures 5c, 5e, supporting information Figures S5c, S5e, S6c, and S6e).

In contrast to the simple structures in the true model and in the isotropic inversions, the results of inverting the anisotropic delays, which include the effects of isotropic and anisotropic structure, contain many artifacts of varying length scales; with some of them reaching dimensions of hundreds of kilometers (Figure 6, supporting information Figures S7–S9). All three cases present similar artifacts indicating that, regarding anisotropy, azimuthal coverage is of secondary importance when dealing exclusively with teleseismic arrivals. The primary factor is the subvertical orientation of the teleseismic ray-paths and their consequential sampling of the slower (faster) directions of regions with subhorizontal (subvertical) fast axes.

The most salient artificial features in the models are: (1) A trench-parallel low-velocity anomaly behind (to the west and opposite the direction of subduction) the slab, (2) A continuation of the previous anomaly around the edge of the slab in the north, (3) low-velocity anomalies in the arc and backarc regions that trend from oblique to perpendicular to the trench, (4) additional low-velocity anomalies near the northern and eastern edges of the model, (5) distortions of the slab shape, and (6) a small high-velocity anomaly directly in front of the slab at depths of 90–200 km. The low-velocity anomaly behind the slab is over 200 km wide between 90 and 200 km depth and while it is present along the length of the slab in the inversion of the original teleseismic distribution, it is concentrated in the northern end of the slab for the rotated and rich azimuth cases. Amplitudes of this anomaly vary between 0.8 and 1.5%. Between 250 and 450 km depth, this anomaly becomes significantly narrower (∼70 km), is more consistent across the three different event distributions, and has amplitudes of 1.5–1.7%. The anomaly directly to the north of the slab edge is most readily distinguishable at 195 km depth and has amplitudes of ∼1%. In the arc and back-arc region, above 250 km, the low-velocity anomalies trend roughly NE-SW, with their SW corner very near the slab, at 1°S to 2.5°S in our reference coordinates with amplitudes that vary somewhat in the different models but are generally of 2% or less. Between 300 and 400 km, the arc/back-arc region exhibits a relatively strong (at

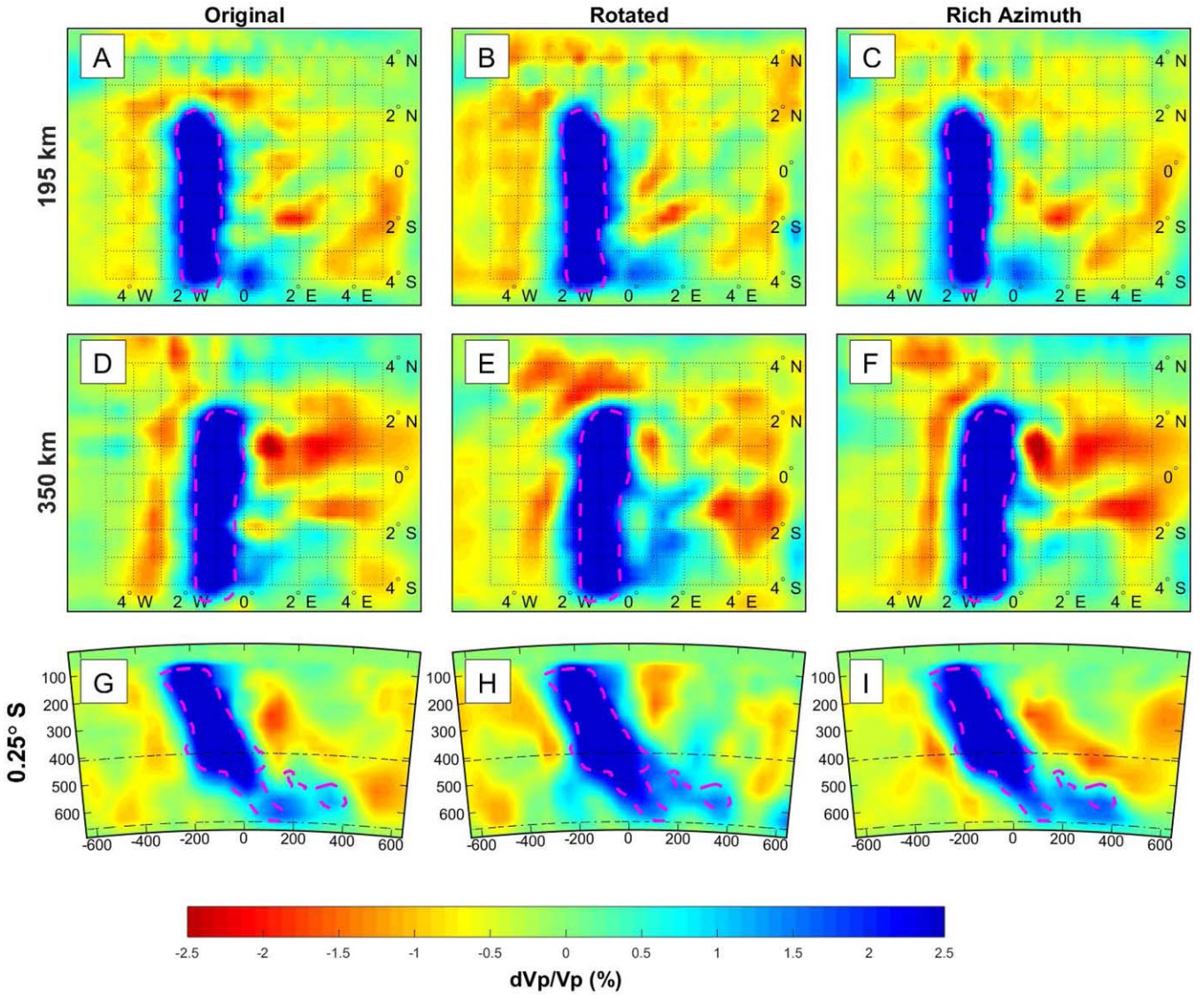

Figure 6. Results of inverting anisotropic delays for the three different teleseismic distributions shown in Figure 4 as indicated on the top of each column. Two depth slices (a–f) and one East-West cross-section (g–i) are shown for each model at depths and latitude indicated on the left of each row. The 1% isovelocity contours for the "true" model are shown as magenta-colored dashed lines for reference. When inverting anisotropic delay times, we observe a number of significant artifacts including moderate distortions of slab shape and the appearance of spatially large low-velocity anomalies. For figures showing four depth slices and two cross sections for each of the three models, the reader is referred to the supporting information.

or above 2%) low-velocity anomaly that has a trench-perpendicular trend and has its western end very near the slab at ~1°N. The slab geometry is recovered fairly well in the three cases but below 500 km it gets distorted in different ways. For the original event distribution, the slab seems to break into three different pieces, while for the rotated case the recovered slab is significantly wider than the input. The slab geometry recovered by the rich azimuth case is reasonably good at all depths. The last anomaly that is consistent across all cases is a small (~100 km in diameter) high-velocity anomaly (1.5–2%) in front of the slab at its southern end. This anomaly is consistently present in all cases above 200 km. Additional low-velocity anomalies occur in the NE and SE corners of the models, and while these can be spatially large they are generally smaller than 1.5% and they are less consistent across the results of the different inversions.

5. Inversions, Local and Mixed Cases

The results presented in the previous section make it clear that many of the artifacts are a product of the steep nature of the teleseismic raypaths, in conjunction with the predominantly subhorizontal orientations

of the fast axes in the shallowest few hundred kilometers of the model. In this section, we explore scenarios where a much greater proportion of the raypaths are subhorizontal, as is the case with local earthquake tomography.

It is common to perform tomography in subduction settings using only local events as sources [e.g., *Zhao et al*., 1992; *Husen et al*., 2000; *Conder and Wiens*, 2006; *Schurr et al*., 2006]. Events occurring within the subducted slab provide good illumination of the slab itself and the arc and back-arc region. Because these rays generally have shallower incidence angles than teleseismic arrivals, and in some cases travel considerable distances near-horizontally through the mantle surrounding the slab, they sample the anisotropic fabric in a very different fashion than the teleseismic events. As a result, artifacts created by the anisotropic structure should be expected to be different. To test this case, we calculated isotropic and anisotropic delay times for 120 events located within the slab. The events were distributed randomly within the slab and span depths from 80 to 350 km. (Figure 7)

Inversion of the isotropic delays produces a very good image of the slab with amplitudes somewhat higher (closer to that of the true model) than in the teleseismic inversions and a very accurate representation of the slab geometry above 300 km. There are no notable artifacts in the recovered model (supporting information Figure S10a—S10c).

The inversion of the anisotropic delays again produces a number of significant artifacts (Figures 8a, 8d, 8g, supporting information Figures S10d—S10f). As expected, these are of a different nature than what we obtained in the teleseismic cases. There is a spatially large, high amplitude anomaly in the arc and backarc region that is widest toward the north and narrows toward the south. This anomaly is large enough to challenge the slab itself as the main feature of the model and is continuous in depth to the deepest area

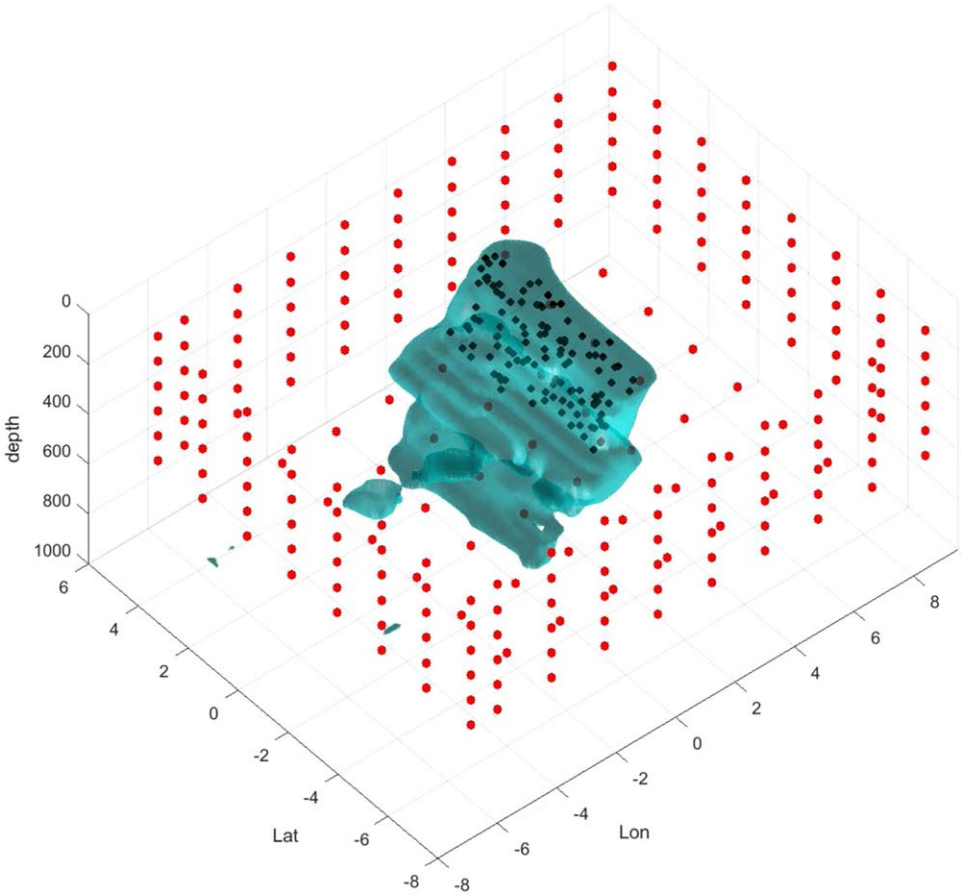

Figure 7. Event distribution for local cases. The figure shows a 3-D rendering of translucent 1.4% fast isovelocity volumes of the true model as well as the local earthquakes used for the "slab" (black dots) and "box" (red dots) local event distributions. Results of inverting delays from these sets of events are shown in Figure 8, and supporting information Figures S10, S13, and S14.

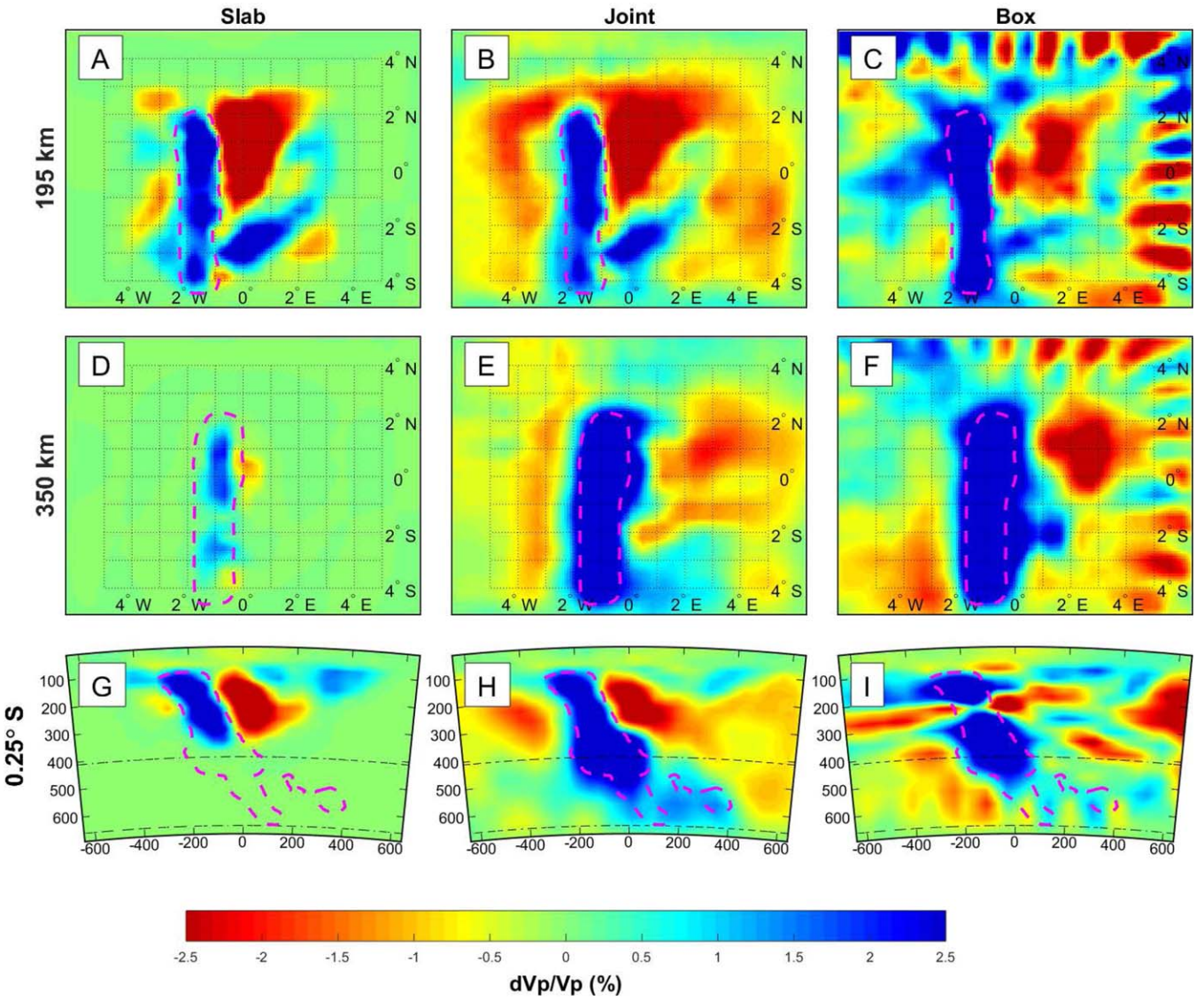

Figure 8. Results of inverting anisotropic delays for the local event distributions shown in Figure 7 ("slab" and "box") as well as the joint inversion of "slab" events and teleseismic events from the "original" distribution (Figure 4) as indicated at the top of each column. Two depth slices (a–f) and one East-West cross-section (g–i) are shown for each model at depths and latitude indicated on the left of each row. The 1% isovelocity contours for the "true" model are shown as magenta-colored dashed lines for reference. Significant artifacts are present in the results for each of the event distributions and appear to be exacerbated by increased ray diversity. For figures showing four depth slices and two cross-sections for each of the three models, the reader is referred to the supporting information.

resolved by the local event coverage. Other large low-velocity anomalies are seen in the SE of the model at shallow depths but are restricted to depths shallower than 160 km. Similarly, a spatially large high-velocity anomaly occurs in the NE part of the model but it has smaller amplitudes (less than 1.5%) and is also restricted to shallow depths. An artificial high-velocity anomaly with substantially high amplitudes (up to 4.4%) but smaller spatial extent occurs to the south of the model in the arc region with a NE-SW trend. In contrast to the teleseismic cases, there are no large anomalies behind the subducting slab.

Given the significant differences (including opposing signs) between the artifacts in the teleseismic and local event cases, we now examine the result of jointly inverting both data sets, to test whether the greater diversity of rays helps reduce the occurrence of artifacts. Specifically, we invert the delays for in-the-slab events together with those for the original teleseismic case. Once again, the inversion of delays derived exclusively from the isotropic velocity structure successfully recovers the subducted slab (supporting information Figure S11) without significant artifacts. The model is almost exactly like that recovered for the

teleseismic case alone with the exception of slightly larger anomaly magnitudes for depths above 300 km. It would be reasonable to expect that inverting the anisotropic delays under this more diverse ray distribution, where both subvertical and subhorizontal raypaths are represented, would be more successful in recovering the isotropic structure as a compromise between inconsistent data constraints. However, the result we obtain is very similar in the upper 300 km to the inversion of the local events alone (Figures 8b, 8h and supporting information Figure S12) with the exception of a large low-velocity anomaly behind the slab, similar to that found for the teleseismic case but with larger amplitudes (2–2.3%) above 250 km. Below 270 km the joint inversion is quite similar to the inversion of the teleseismic delays alone, the main difference being a slight reduction of the amplitude of the low-velocity artifacts. Interestingly, instead of an improvement of the image quality, we observe that the joint inversion produces an exacerbation of artifacts in the upper 300 km of the model.

To gain some additional insight, we perform one more numerical experiment with an event distribution that, while completely unfeasible, is nonetheless informative. We place 204 events regularly spaced on a rectangular box just within the margins of the model domain, with lateral spacing of 200 km and vertical spacing of 100 km from 100 to 600 km depth (Figure 7). Additionally, 42 events are located at the bottom of the box at a depth of 650 km to provide subvertical illumination. This hypothetical distribution provides a degree of sampling richness and evenness that is impossible to reproduce in practice. The purpose of this experiment is to test if with this idealized event distribution we are able to recover the isotropic anomalies. Once again, the recovery of the isotropic structure from the isotropic delays is entirely satisfactory both in terms of geometry and amplitude of the subducted slab anomaly (supporting information Figure S13).

Perhaps counterintuitively, the image produced by inverting the anisotropic delays is still plagued with artifacts (Figures 8c, 8f, 8i and supporting information Figure S14). In stark contrast to the simple structure in the true model, the inversion results exhibit a complicated array of anomalies, many of them with length scales on the order of 100 km or less. The edges of the model to the north and east are characterized by a pattern of small anomalies that alternate between neutral and high or low-velocity anomalies with amplitudes larger than 3% above 400 km depth. Although these anomalies are alarming, they would bear little significance on the interpretation of any model since they could readily be dismissed by virtue of their unnatural appearance and their location being restricted to the edges of the model. Of greater concern are the many artificial anomalies in the interior of the model. While the slab is generally recovered in the correct location, its shape is distorted more than in any of the previous model. At ~250 km depth, its northern half appears discontinuous with depth as if a horizontal tear was dissecting it. Above 400 km there are various artificial low-velocity anomalies with spatial dimensions on the order of 200 km. These anomalies have peak amplitudes of ~3% or larger and have little continuity in the vertical direction; their shape and location changes considerably at different depth intervals. Below 400 km the artifacts are less severe (likely owing to the much smaller amount of anisotropy in the transition zone) and are mostly reduced to a low-velocity rim surrounding the slab with amplitudes of 1–1.7%. From this experiment we infer that, for regional, upper mantle scale body-wave tomography, no amount of richness in ray coverage is immune to the kind of complex anisotropy patterns that can be expected around subduction zones. Indeed, it appears that increasing the diversity of incidence angles and azimuths represented by the ray coverage is likely to exacerbate the occurrence of artifacts, rather than ameliorating it. A related result is the relationship between ray diversity and data misfit. Table 1 shows that while isotropic delays are fit equally well for all of the cases we have considered, the misfit varies significantly for the inversions of anisotropic delays. Event distributions that result in richer, more diverse, raypath ensembles produce significantly higher data misfits.

Table 1. RMS Data Misfit for Different Event Distributions and Prescribed Anisotropy Fields

Case	RMS Isotropic Delays (ms)	RMS Anisotropic Delays (ms)
Original teleseismic	45	147
Rotated teleseismic	45	142
Rich Azimuth teleseismic	51	187
Joint teleseismic + local	47	189
Local	42	186
Box	59	324
True anisotropy		31
Coarse 1		46
Coarse 2		58
Depth-averaged magnitudes		81
Ad hoc toroidal		107
Coarse 3		123
Behind the Slab		143
SKS 100-300		145
SKS 100-200		146

6. Addressing the Problem Using Prescribed Anisotropy Fields

In the previous section, we have shown that anisotropy created by complex mantle flow fields around subduction zones can result in potentially serious artifacts in isotropic tomography that could have important implications for interpretation. Here, our geodynamically based, subduction-zone-specific study is in agreement with what has been found by previous studies focusing on different settings or on generic scenarios. To address the issue of anisotropic traveltimes, the most seemingly straightforward approach would be to try to invert for anisotropy as well as isotropic velocity. Indeed this approach has been used in some settings [e.g., *Eberhart-Phillips and Reyners*, 2009; *Tian and Zhao*, 2012; *Wang and Zhao*, 2013]. However, there are problems with this approach as a general solution that pertain to the availability of sufficiently dense data sets. The challenge of resolving anisotropic structure is great, given that isotropic tomography is already an underdetermined problem and additionally inverting for anisotropy direction and strength quadruples the number of unknowns even when assuming hexagonal symmetry. While a fully anisotropic inversion may well be feasible in some areas, many subduction zones of great scientific interest and with documented high anisotropy do not exhibit abundant intraslab seismicity; which makes it impossible to produce the kinds of data sets that would be likely to constrain the anisotropy field. This is especially true if the goal is to image large areas including the arc and backarc regions and if the depth interval of interest is the entire upper mantle.

An alternative and attractive solution is to incorporate the anisotropy field as prescribed parameters on the model. That is to say, invert for isotropic structure under the constraint of an anisotropy field that is taken as known a priori. This is achieved by including the anisotropy field in the forward modeling: at each iteration, the delays are recalculated with respect to a velocity model composed of the isotropic structure produced in the previous iteration plus the prescribed anisotropy field. For the first iteration, the delays are recalculated by imposing the prescribed anisotropy field on the 1-D reference velocity model. This approach effectively isolates the delays from the isotropic velocity anomalies making the data set more consistent with the assumptions built into the inversion.

While this approach may seem unorthodox, we note that assuming an a priori anisotropy structure is indeed an accepted practice. Current state of the art is to prescribe a zero-anisotropy condition. What we are proposing is we may now have sufficient information (from geodynamic modeling and SKS splitting observations) to generalize this methodology by trying different approximations to the anisotropy field.

An initial benchmark test consists of prescribing the true anisotropy field for our synthetic model. As is to be expected, the inversion is able to recover the true isotropic structure very accurately (supporting information Figure S15) and the rms misfit is comparable to that obtained by the inversion of the isotropic delay times. No significant artifacts are observed, with only spurious low-velocity anomalies with amplitudes smaller than 0.5% comparable to the inversions of isotropic delay times. While for any real-world scenario, the 3-D anisotropy field will never be exactly known, we perform this exercise as an end-member scenario against which we can compare the efficacy of inversions performed prescribing approximated anisotropy structures.

Beyond this benchmark, we test eight different models that all represent different approximations to the true anisotropy field with various degrees of accuracy. The approximate anisotropy models can be separated into two classes. The first class was built by starting from the known anisotropy field and coarsening or decimating it to various degrees to build increasingly rough approximations. The second class is comprised of ad hoc models that aim to emulate the characteristics of the true model in a simplified way based either on assumptions loosely based on the geodynamic model (Behind Slab and ad hoc toroidal) or solely on the SKS splitting pattern (SKS100300, SKS10020). Our approximate anisotropy exercises are all carried out using the "original" teleseismic event distribution. In order to maintain the length and scope of this paper reasonable, we do not test every permutation of approximate anisotropy field and event distribution. In the following, we show that using nonzero anisotropy approximations can produce useful results even when they deviate significantly from the true anisotropy field, and that there are means to evaluate whether a particular approximation is better or worse than the standard zero-anisotropy approximation.

6.1. Models Derived Directly From the True Anisotropy Field

There are four models in this class. Three of them, that we refer to as Coarse 1, 2, and 3, were produced by restricting the values of the azimuth and zenith angles to sets with intervals of 30, 45, and 90°, respectively,

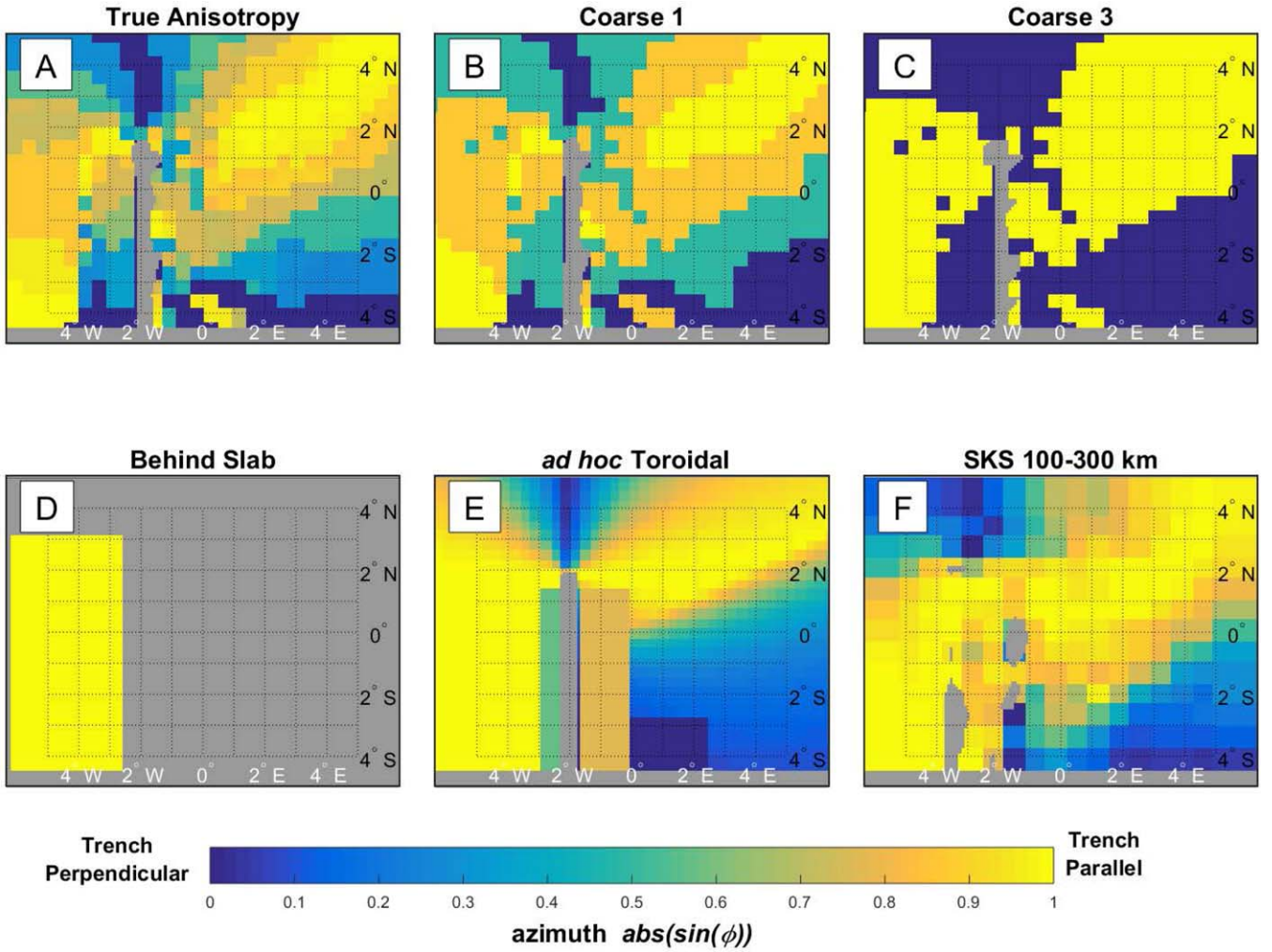

Figure 9. Azimuth distribution for six different anisotropy models used as a priori constraints on the tomographic inversions. Model names are indicated above each plot. All plots represent depth slices at 195 km depth.

while the anisotropy magnitude values were restricted to sets with 1.5, 2, and 3% intervals, respectively (Figures 9b, 9c, 10b, 10c, 11b, and11c). The fourth model in this class was produced by maintaining the azimuth and zenith values from the true model but setting the anisotropy fraction at each point to the average of all true values at the corresponding depth.

The result of inverting using Coarse 1 as the prescribed anisotropy field are almost identical to those produced by the benchmark case (Figures (12 and 13), and supporting information Figure S16). Coarse 1 does produce a few more small, low-amplitude, low-velocity anomalies; but for practical purposes the two models are equivalent. That is to say, neither model contains artificial anomalies that are large enough in either spatial extent or amplitude to warrant interpretation.

The inversion using the Coarse 2 approximation does produce some artifacts that could be considered significant. In particular, there is a linear low-velocity anomaly near the northern boundary of the model and, more importantly, a low-velocity anomaly (∼1%) in the arc/backarc region that dips opposite the slab (supporting information Figure S17). The progression toward more artifacts continues with Coarse 3 (Figures 12f, 13f, and supporting information Figure S18). The corresponding inversion result contains artificial anomalies that coalesce into large bodies that are well above the expected resolution for this model (i.e., they would seem like reasonable targets for interpretation). It is worth noting however that even though Coarse 3 is very blunt approximation to the true anisotropy, the artifacts produced in this case are less severe than those produced under the no-anisotropy approximation (Figures 12 and13). The last model in

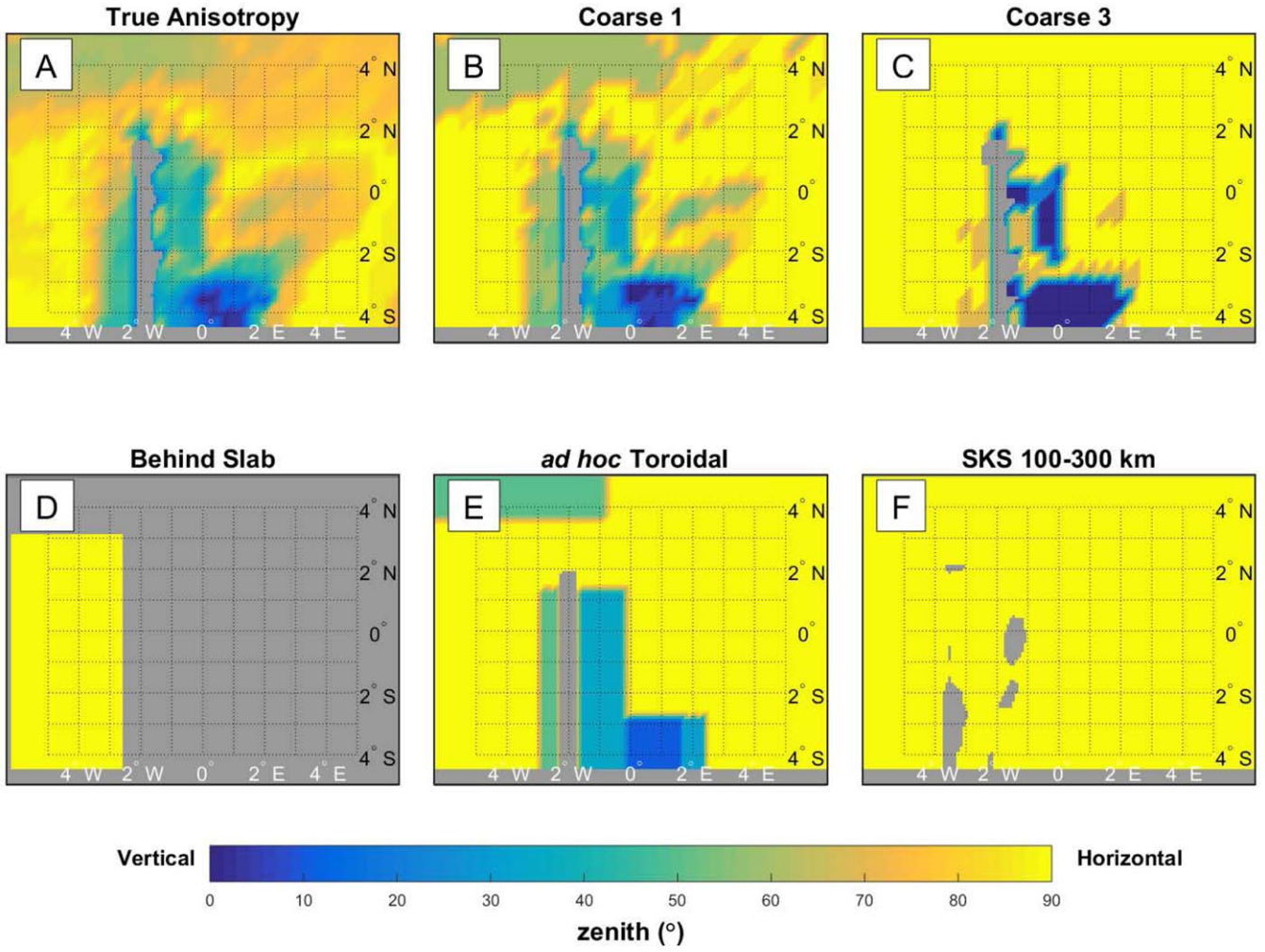

Figure 10. Zenith distribution for six different anisotropy models used as a priori constraints on the tomographic inversions. Model names are indicated above each plot. All plots represent depth slices at 195 km depth.

this class (depth averaged anisotropy magnitudes) produces artifacts that are comparable to those of Coarse 2, if somewhat larger. The most notable ones are a linear low-velocity anomaly behind the slab and low-velocity anomalies in the arc/backarc region, all of which reach their largest amplitudes (∼1.5%) between 300 and 400 km depth (supporting information Figure S19).

6.2. Ad Hoc Approximation Models

In this suite of tests, we approximate the anisotropy field for either the whole model or a particular region of interest without making direct use of the anisotropy values of the input model, but taking into account the general features of the anisotropy produced by the geodynamic model and the synthetic SKS splitting results. The first approximation focuses on the area behind the slab, as this is where the most significant artifact is observed for the teleseismic cases. The model was built by assuming anisotropy is distributed in two layers in the subslab mantle. A shallow layer within the depths of 90 and 175 km is characterized by trench perpendicular fast axes (Figures 9d, 10d, and 11d) and is underlain by a layer with trench-parallel fast axes that extends from 175 to 360 km depth. The magnitude of anisotropy in each layer was chosen such that a vertically traveling shear wave would experience splitting times of 0.2 s with the fast polarization direction being trench perpendicular, similar to the SKS predictions for the input model. Not surprisingly, the corresponding inversion result is very similar to the zero-anisotropy case everywhere except behind the slab (Figures (12 and 13), and supporting information Figure S20). There, the artificial anomaly we had observed is now absent. This exercise suggests that prescribing simple anisotropy structures in limited

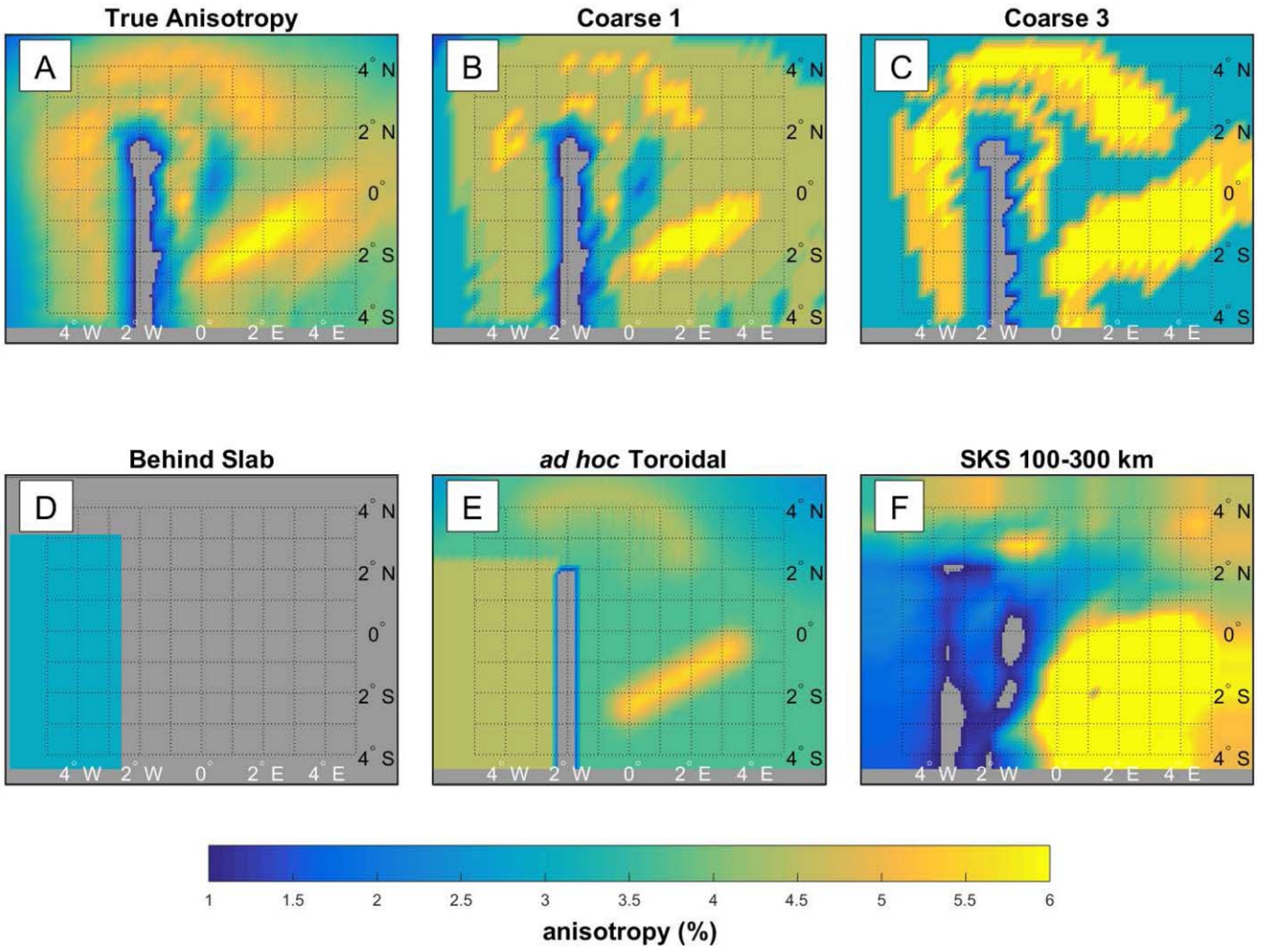

Figure 11. Distribution of anisotropy magnitude (in %) for six different anisotropy models used as a priori constraints on the tomographic inversions. Model names are indicated above each plot. All plots represent depth slices at 195 km depth.

regions of the models may be an easy and effective way of exploring whether specific anomalies of interest could be artifacts produced by anisotropy.

We refer to the next model in this series as ad hoc toroidal. The anisotropy in this case is relatively complex in that it tries to incorporate the different components of flow that are present in the real model. At the same time, the model is very simplified in that most of these components are represented by rectangular blocks that are homogeneous in terms of anisotropic parameters (Figures 9e, 10e, and 11e). The components of the model are:

1. Entrained mantle above and below the slab, with mostly downdip anisotropy.
2. The area behind the slab with a pattern similar to that of the previous model.
3. A toroidal pattern around the northern edge of the slab with azimuths being tangential to the slab edge. Note that this pattern is only similar to first order to the pattern found on the true model.
4. A region where the toroidal pattern has a small upwelling component.
5. A transition from toroidal to trench perpendicular fast axes in the arc and backarc region.
6. A region with subvertical fast axes near the southern end of the model (middle of the slab) where flow is predominantly poloidal.

This approximated anisotropy field is fairly successful in removing the series of low-velocity anomalies that begin behind the slab, continue around its edge and culminate in the NE-SW trend (Figures 12e, 13e, and

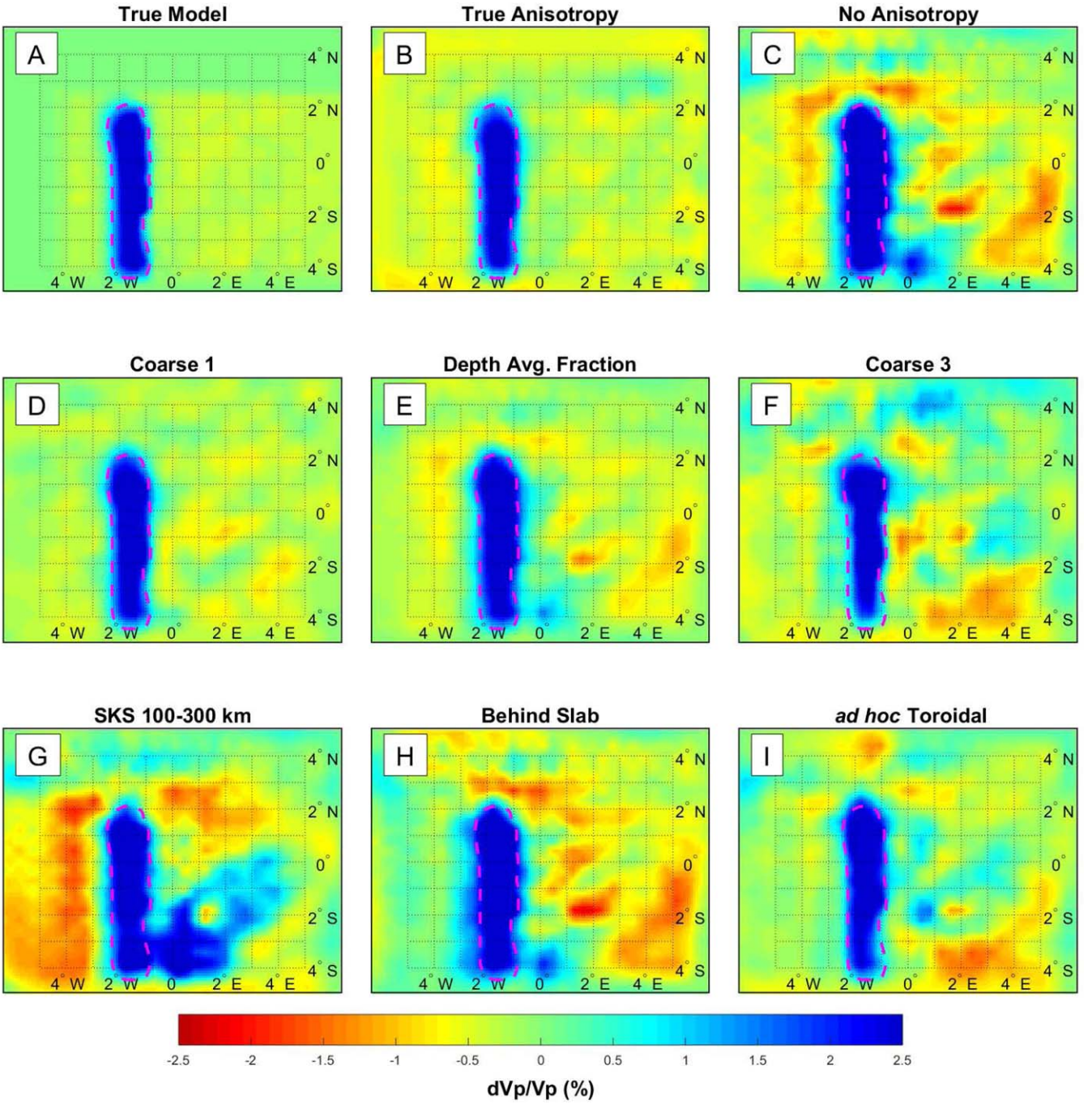

Figure 12. Results of inverting anisotropic delays while using different anisotropy fields as a priori constraints (b–i) and "true" model for comparison (a). For Figures 12b–12i, the name of the anisotropy field used in each case is indicated above each plot. The 1% isovelocity contours for the "true" model are shown as magenta-colored dashed lines for reference. All plots represent depth slices at 195 km. The severity of the artifacts varies according to the accuracy of the approximate anisotropy field used. For figures showing four depth slices and two cross sections for each of the models, the reader is referred to the supporting information.

supporting information Figure S21). Above 250 km depth, artificial anomalies are relatively small and not organized into large coherent features, which would render them less attractive for interpretation. While some significant low-velocity anomalies remain and a few small high-velocity artifacts are introduced, the model represents a considerable improvement over the zero-anisotropy case and outperforms the Coarse 3 model in quantitative assessments as will be discussed in the next section.

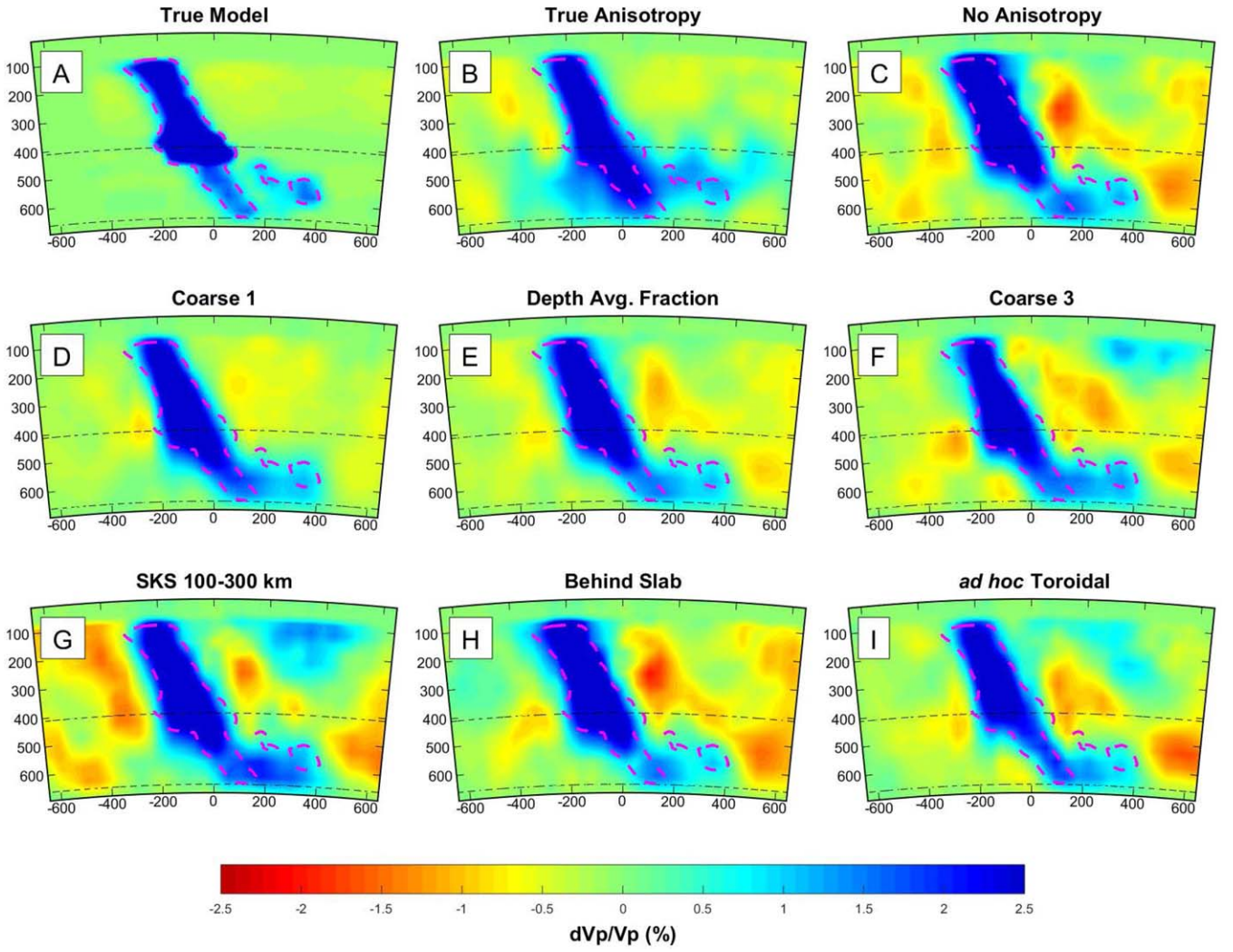

Figure 13. Results of inverting anisotropic delays while using different anisotropy fields as a priori constraints (b–i) and "true" model for comparison (a). For Figure 13b–13i, the name of the anisotropy field used in each case is indicated above each plot. The 1% isovelocity contours for the "true" model are shown as magenta-colored dashed lines for reference. All plots represent East-West cross-sections at 0.25°S. The severity of the artifacts varies according to the accuracy of the approximate anisotropy field used. For figures showing four depth slices and two cross sections for each of the models, the reader is referred to the supporting information.

The two remaining models in this class were built with a focus on the pattern of synthetic SKS splitting, assuming the synthetic splitting observations are produced by a single layer of vertically congruent anisotropy. At each point, the fast axis is horizontal and its azimuth is the same as the fast polarization direction (extrapolated outside the array footprint using the nearest neighbor method) (Figures 9f and 10f). The anisotropy magnitudes (Figure 11f) are defined such that they would produce the splitting delay observed at each station if the arrival was vertical. We try two different cases: In both, the top of the anisotropic layer is at 100 km, while the depth to the bottom of the anisotropic layer is 300 and 200 km, respectively. The underlying assumption would be that the mantle flow is predominantly horizontal and that the anisotropy is concentrated in the asthenosphere.

The inversion results for the two splitting-based models are essentially indistinguishable (supporting information Figures S22 and S23), indicating that the choice of the thickness of the anisotropic layer has little to no influence on the results. The recovered models for these cases are significantly different from all the other models we have considered thus far (Figures (12 and 13), and supporting information Figures S22, S23). Interestingly, the low-velocity anomaly behind the slab is exacerbated in this case rather than abated, given that SKS splitting times in this region of the model are relatively small (owing to the contrasting effects of overlapping trench-parallel and trench-perpendicular fast axes in the true model). The models also contain

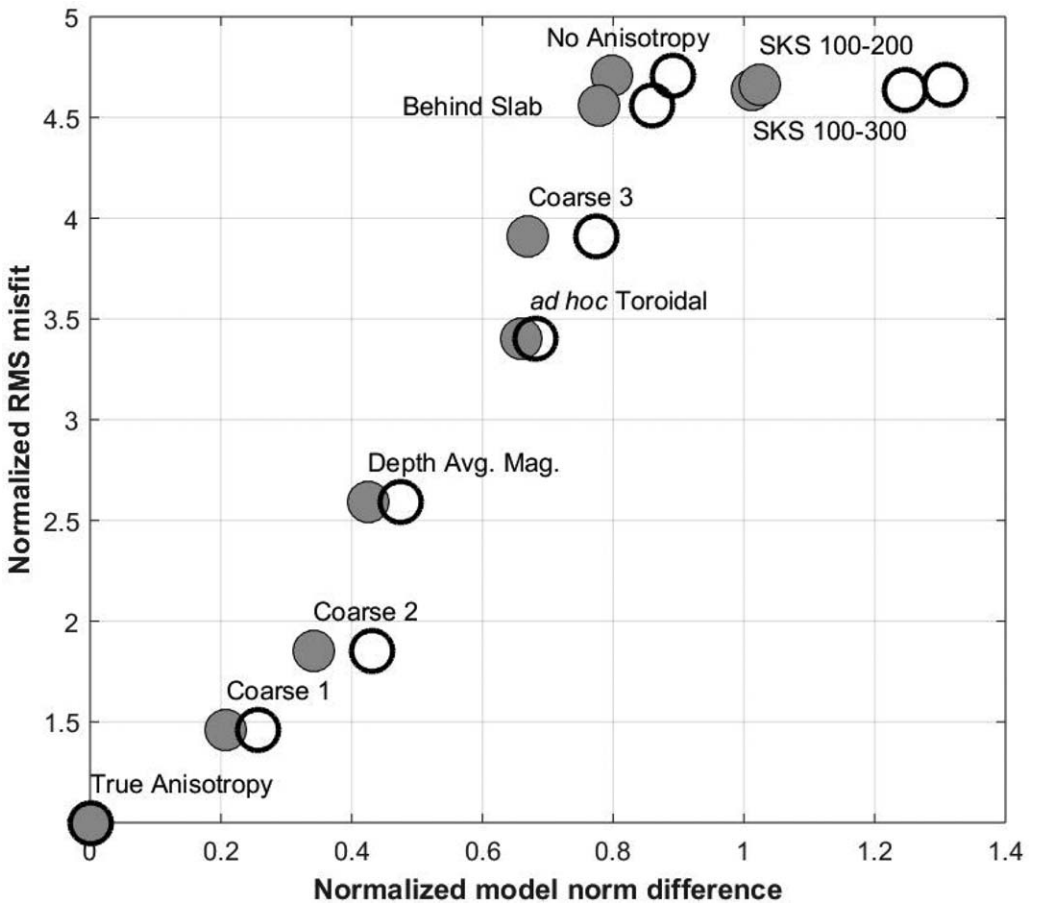

Figure 14. Normalized RMS misfit versus normalized norm difference for various models with respect to the model resulting from prescribing the "true anisotropy" field. The names of the approximate anisotropy field are indicated next to the corresponding symbols. Filled symbols correspond to calculations using the entire models, open symbol correspond to calculations that use only depths from 0 to 250 km.

high-velocity artifacts that are more significant in terms of spatial dimensions and amplitudes (>2%) than those found in any of the previous models. Both the high and low-velocity artifacts in these models are in most cases large enough to be considered above the resolution could be described as first-order features of the model (Figures (12 and 13) and supporting information Figures S22, S23). The results of these inversions remind us that station-averaged shear wave splitting observations may not provide a full picture of the anisotropy field in the subsurface, since they do not reflect downdip anisotropy or vertically incongruent fast axes. This should not be taken to mean that the splitting observations are not useful for inferring the 3-D anisotropy field. It is quite possible that, at least locally, the assumption of single-layer anisotropy being responsible for the splitting observations is valid. Additionally, when implementing the "prescribed anisotropy" approach on real data, it is imperative that any approximate anisotropy field that is used be consistent with the splitting observations.

6.3. Quantitative Comparison of Approx. Anisotropy Models

In Figure 14 we represent each of the models discussed in this section in a way that helps us assess their relative success both in explaining the travel time observations and in producing an isotropic velocity model that closely resembles the input model. Most of the models fall along a linear trend that connects our two reference cases: the benchmark case (where the true anisotropy is prescribed) and the zero-anisotropy case that represents the standard way of doing teleseismic P-wave tomography. For the first class of models (those derived directly from the true model), the data misfit and accuracy of the recovered model becomes degraded as the approximation becomes coarser, as is to be expected (Figure 14). The highest fidelity approximation (Coarse 1), despite errors in orientation of up to 15° in azimuth and dip, represents an enormous improvement in data misfit and model accuracy, with respect to the standard zero-anisotropy case.

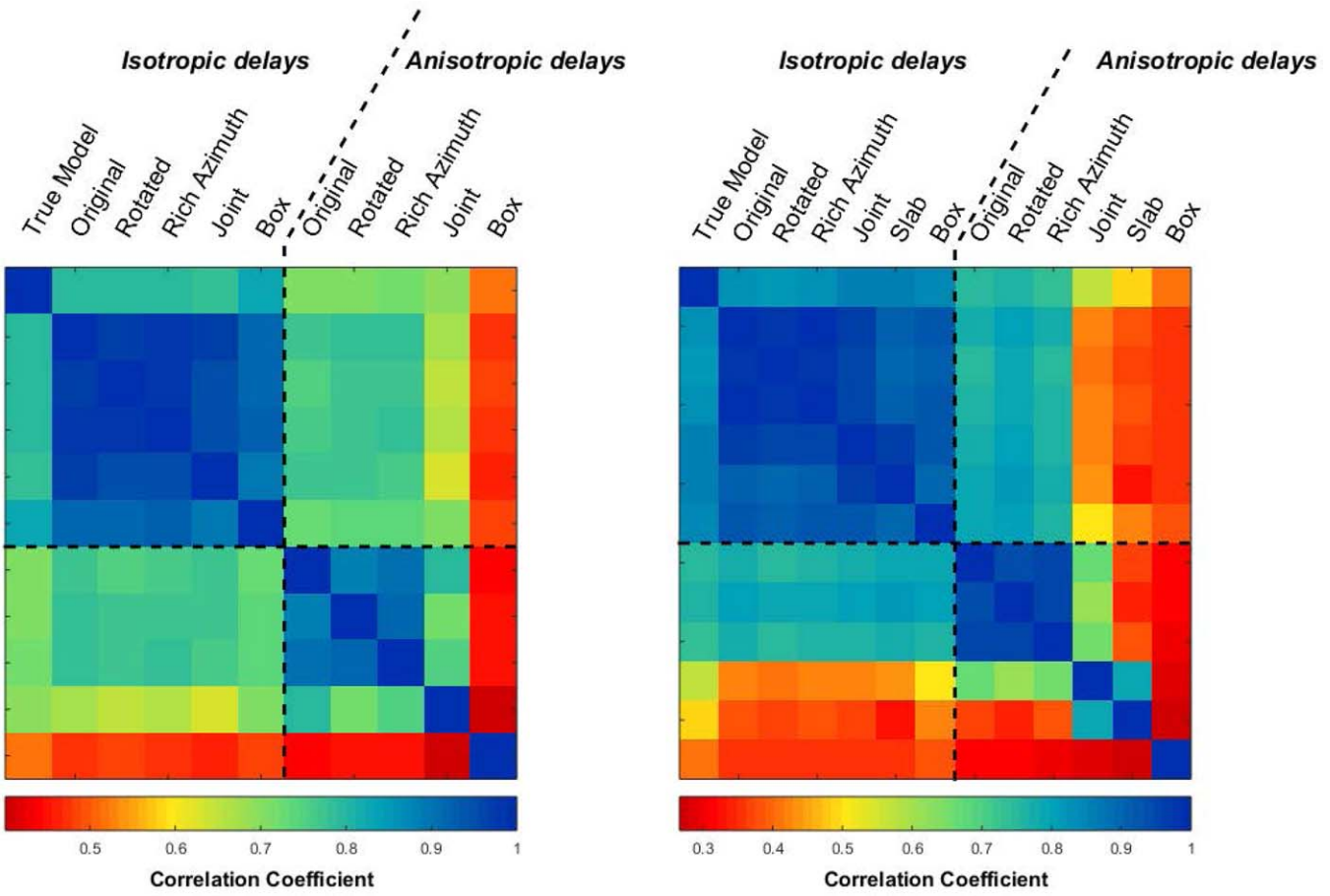

Figure 15. (left) Model correlation matrices for whole models and (right) only the uppermost 300 km. Dashed lines separate models resulting from the inversion of isotropic and anisotropic delays. All models resulting from inverting isotropic delays show strong correlations with each other. The same is true of the inversions of anisotropic delays stemming from the three teleseismic event distributions.

The same could be said about the second highest fidelity model that contains errors in orientations of over 20° and in anisotropy magnitude of up to 1%. We note that even though Coarse 3 is a very blunt approximation to the anisotropy field, it produces an appreciable improvement in data misfit with respect to the zero-anisotropy approximation (Figure 14). The abundance of artifacts is also reduced and those artifacts that remain (or are newly introduced) are somewhat smaller and less attractive as interpretation targets.

Two of the models from the second (ad hoc) class also fall in the linear trend described above. Figure 14 shows that the case with anisotropy restricted to the region behind the slab shows improvements in data misfit and artifact abundance, albeit very modest ones. Qualitatively, however, these small improvements are significant given that this approximation achieves its goal of eliminating a large, trench parallel low-velocity anomaly from the model (Figures 12h, 13h, and supporting information Figure S20). This model would show that anisotropy is sufficient to produce the time delays that generated the anomaly and that elevated temperature or volatile content is not required by the data. In addition to explaining traveltimes slightly better than the zero-anisotropy model, this case would have the advantage of being at least locally consistent with SKS splitting observations.

In contrast to the previous case, the improvements afforded by the ad hoc toroidal model are quite considerable. Indeed, this model outperforms Coarse 3 in terms of both data misfit and artifact reduction (Figure 14). Each of the models we have considered so far in this section move away from the zero-anisotropy case and toward the true-anisotropy case in the plot of Figure 14. The models based exclusively on the synthetic shear wave splitting observations are the only ones to fall off this trend. While this model achieves a very small reduction in data misfit, the abundance of artifacts with respect to the zero-anisotropy reference is

increased. If we restrict our metrics to the shallowest 250 km of the model, where many important processes related to slab dehydration take place, the artifact problem is even worse for these models (Figure 14). In contrast, for the same cutoff depth, the ad hoc toroidal model compares even more favorably with the Coarse 3 case (Figure 14).

We close this section by noting that for many of the cases presented there are a number of subsequent tests that could be performed to determine the sensitivity of the result to various parameters that differ in a case-by-case basis. Such extensive testing would go beyond the scope of the current paper. Here, we treat this suite of tests simply as a proof of concept to show that the use of prescribed nonzero anisotropy fields may be a viable alternative and yield useful information where a full inversion for anisotropy is simply not feasible.

7. Discussion

We can summarize the results of our zero-anisotropy inversions by taking the correlation coefficient between pairs of models as a simple measure of their similarity. This is presented visually in Figure 15. We note that there is mostly a bimodal distribution of correlation coefficients between the true isotropic velocity structure and the inversion results (for the complete models, Figure 15). A first group of models with high correlation coefficients ($\sim$0.8) includes the inversions of isotropic, while the results of inverting anisotropic delays without anisotropy constitute the second group of models with lower correlation (0.7) to the true model. The correlation coefficient between the true model and the inversion of anisotropic delays with the "box" distribution of events is only 0.5.

An important observation is that the results of inverting anisotropic delays from different teleseismic event distributions are highly correlated with each other (x = 0.97–0.98). This is a simple quantification of the observation that very similar artificial anomalies were produced in each of these cases. Two important corollaries can be stated from this result: (1) In P-wave teleseismic imaging, azimuthal coverage does not have a first-order effect on the occurrence and distribution of anisotropy-related artifacts; (2) Artificial anomalies can be expected to be robust with respect to the set of events used, and thus appear to be a reliable representation of the subsurface structure. The most prominent artificial anomalies in the teleseismic cases were slow in nature and could be interpreted in terms of physical processes characteristic of subduction zones such as mantle hydration and melt production, migration, and accumulation.

We note that, in a study of the Cascadia subduction zone, *Eakin et al.* [2010] observed a correlation of low-velocity velocity anomalies in the tomography model and high shear-wave splitting times. To us, this suggests one possible occurrence of anisotropic structure being mapped into low-velocity anomalies in an isotropic velocity model.

The good correlation between the inversions of delays from intraslab events and a combination of intraslab and teleseismic events (in the appropriate depth range, Figure 15, right) shows that, in mixed event distribution cases, the effect of anisotropy on local delays has a predominant effect on the distribution of artifacts in the upper $\sim$350 km of the model. In contrast to the teleseismic cases, local events produce very significant high-velocity artifacts (supporting information Figure S10 and S12). These high-velocity anomalies resemble what could be interpreted as delamination events or Rayleigh-Taylor instabilities occurring in the back arc.

To explore how these artificial anomalies may affect quantitative interpretations, we focus on the large low-velocity anomaly the low-velocity anomaly that occurs behind the slab and surrounds the northern edge of the subducting slab at shallow depths (Figure 6, and supporting information Figures S7–S9). The magnitude of this anomaly, at its core, is on the order of 1.5%. If such a velocity anomaly were attributed to temperature, at a depth of 150 km, we would erroneously infer a temperature anomaly of $\sim$120°K using $\partial \ln Vp/\partial T = -0.8/100^{\circ}K$ [*Cammarano et al.*, 2003]. Going a step further, we can calculate the associated density anomaly ($\sim$12 Kg/m^3 using an upper mantle density of 3300 kg/m^3 and a thermal expansion coefficient $\alpha = -3 \cdot 10^{-5^{\circ}}\mathrm{K}^{-1}$) and use Airy isostasy to predict over 600 m of excess topography to balance the load of a 150 km thick layer of hot, buoyant material. Alternatively, a 1.5% velocity reduction could be interpreted to indicate to the existence of $\sim$1% partial melt [*Hammond and Humphreys*, 2000].

Thus far, we have focused on the characteristics of the recovered models for each of the cases tested. We now consider the variations in data misfit for each of these scenarios (Table 1). The inversion of isotropic delays yields low RMS misfits, indicating that the algorithm is capable of producing a model that provides a very good fit to the data. In these cases, the values we obtain for RMS misfit are comparable to what the picking error would be in real 1 Hz data. In contrast, when inverting anisotropic delays, there is an increase in the RMS misfit by a factor of 3–4 for most cases. In the last hypothetical case tested, with an idealized local event distribution, the RMS misfit climbs to over 320 ms, representing a ∼sixfold increase over the corresponding isotropic case. These results show that when inverting anisotropic data under the assumption of isotropy, for regional-scale subduction models, increasing the diversity of raypaths does not preclude the occurrence of anisotropy-related artifacts. As the data become more abundant and rich, they also become more inconsistent with purely isotropic structure. This would then require heavier regularization and lead to greater data misfit, greater amounts of artificial structure, or both. We also note that there is a risk of interpreting the correlation between the richness of the data and the complexity of the resulting models as increasing resolution of complex isotropic structure, rather than as a greater abundance of artifacts.

While the object of this paper is to examine inversions of anisotropic synthetic data, the success of the inversions of the isotropic synthetic data is also a result worthy of attention. Our inversions of isotropic data are identical to the synthetic tests the community commonly uses to test the reliability of tomography models. Our isotropic inversion results imply that typical synthetic tests will lead to excessive confidence on the models, since large artifacts are absent. From such tests, one would conclude that large anomalies in the inversion results are required by the data. This erroneous conclusion would then justify the interpretation of anomalies that could be anisotropy-related artifacts.

Although the synthetic SKS observations we calculate for our models are similar to real observations (supporting information Figure S2), we find a small number of splitting times above 2.5 s which are very rare in real observation. If, for example, diffusion creep plays a bigger role in accommodating upper mantle deformation than we have assumed in our modeling, it is possible that for parts of the model, the anisotropy we use in our numerical experiments is a high estimate. However, even if this is the case, our results have significant implications for real subduction zone imaging. The artificial anomalies we observe are large enough that any significant fraction of these would significantly affect results, producing a considerably distorted image of the subsurface. In this paper we have focused on the effects of anisotropy on P-wave imaging. The mantle model on which we have based our synthetic tomography experiments exhibits lateral heterogeneities in direction-dependent Vs and Vp/Vs_1 ratio that are comparable to those for Vp. While our results suggest that Vp/Vs_1 estimates from tomography will be affected by Vp artifacts, the Vs case is more nuanced. The effects of anisotropy on S-wave delays depends on the polarization used to make the measurements: While S delays picked on the S_{slow} direction (perpendicular to the fast polarization direction determined by shear-wave splitting) have a similar sensitivity to anisotropy than P waves, delays picked in the S_{fast} direction are less sensitive to anisotropy and may provide a more faithful indication of isotropic velocity variations [e.g., *Toomey et al*., 1998; *Hammond and Toomey*, 2003].

Although the issue of anisotropy affecting isotropic tomography models has been raised by previous publications [e.g., *Kendall*, 1994; *Blackman et al*., 1996; *Grésillaud and Cara*, 1996; *Blackman and Kendall*, 1997; *Sobolev et al*., 1999; *Wu and Lees*, 1999; *Sieminski et al*., 2007], relatively little attention is presently given to anisotropy in body-wave imaging of the mantle. Hence, isotropic tomography remains the primary means of imaging subduction zones. A leading reason for this may be the perceived lack of a practical, feasible, and readily applicable alternative. As a very first step, we join others in stressing that great caution and restraint should be exercised when interpreting isotropic models of subduction zones, especially where anisotropy is known to be significant (from SKS splitting, for example).

In this study, we have tested an approach based on prescribing the anisotropy field and shown that this may be a useful compromise between isotropic and fully anisotropic tomography. The success for the Coarse 1 and Coarse 2 approximations demonstrate that the anisotropy field need not be matched exactly to obtain excellent results. Therefore, an anisotropy field that matched the overall character of the SKS observations, even if not the detailed short-wavelength variations, would likely be more than adequate to account for the variations in travel times that are observed in teleseismic studies. What is more, it would not be necessary to match the anisotropy field in all regions of the model to obtain useful results. The "behind slab" case shows that specific anomalies can be addressed by inserting rather simple and localized

anisotropy structure into the model. This would perhaps be a good place to start when applying this approach to real data. From testing an individual anomaly, the complexity of the prescribed anisotropy could gradually be increased, and we suggest that at each step the data misfit and the model norm can be used to gauge whether or not results are improving.

As mentioned in a previous section, a prerequisite for using a particular approximate anisotropy model as a prior constraint on a real-data inversion would be for that approximate anisotropy field to be consistent with SKS splitting observations. However, we note that for the anisotropic input model we have tested, using the SKS splitting results as sole guide to build an approximate anisotropy field does not produce a satisfactory result. This is partly due to the fact that there is significant dipping anisotropy in our input and the assumption that restricts fast axes to the horizontal plane does not hold. Additionally, we have nonvertically congruent anisotropy behind the slab which produces an additive effect for time delays (subvertical raypaths travel along a slow direction for both layers), but a destructive effect for SKS splitting (fast polarization directions are orthogonal). It may very well be the case that, at least locally, in real subduction zones the assumption of subhorizontal and vertically congruent fast axes is valid, and thus using the SKS splitting observations to build an approximate anisotropy field may produce useful results.

We also show that the severity of the artifacts and the data misfit are sensitive to the accuracy of the approximation. If our approximations are based on predictions from geodynamic modeling, we may be able to use the traveltime data (in addition to the SKS splitting observations) to constrain some of the parameters used in the modeling. The assumption of A-type or B-type olivine fabric, the chosen viscosity structure, and the parameters used to convert finite strain to LPO formation would have a significant influence on the predicted anisotropy structure such that if the wrong parameters are chosen, it is likely that the resulting approximation would not produce a better tomography result. In this way, the geodynamic modeling and the anisotropic tomography can be seen as constraining each other. Already thermomechanical models are checked against SKS splitting [e.g., *Becker et al*., 2006a; *Faccenda and Capitanio*, 2012, 2013; *Alpert et al*., 2013] and radial anisotropy observations, the addition of travel-time tomography as a constraint could lead to integrated, internally consistent models of mantle isotropic velocity structure, anisotropy fields, and dynamic evolution. While this is admittedly ambitious and optimistic, it is an exciting prospect that, in our opinion, should be pursued with vigor.

Finally we address the fact that it will be prohibitively difficult in most, if not all cases, to uniquely constrain the anisotropic structure in an area with a complex mantle flow field such as subduction zones. However, since we have shown that is possible to see when an assumption about the anisotropy field is not consistent with the data (even when consisting with SKS splitting), it will be possible to eliminate hypotheses about mantle flow by testing their predictions against the travel-time data, in addition to any shear wave splitting results.

8. Conclusions

We carried out a suite of synthetic P-wave tomography experiments based on a self-consistent model of thermal (isotropic) velocity structure and seismic anisotropy derived from micro-macro mechanical modeling of subduction rollback. Travel time delays were calculated for this model and a number of different event distributions. Inverting these delays under the assumption of isotropy resulted in significant artificial anomalies, as time delays caused by the anisotropic structure can only be mapped into the models in terms of isotropic velocity anomalies.

For teleseismic event distributions, large low-velocity artificial anomalies occur behind the subducting slab, around its edge and in parts of the arc and backarc region. This result is largely insensitive to azimuthal coverage and to the angle between the dominantly-sampled backazimuth and the trench-parallel direction. If interpreted in terms of thermocompositional parameters, these anomalies could represent $\sim$120 K of excess temperatures or $\sim$1% partial melt. The inferred temperature anomaly, would lead one to predict $\sim$600 m of mantle-supported excess topography.

Simulating local earthquake tomography produced a different set of artifacts given that raypaths sampled the anisotropic structure very differently from teleseismic rays. Joint inversion of local and teleseismic delays

was not successful in eliminating or even reducing the artifacts, and artificial anomalies were still plentiful when we used an unreasonably rich and diverse ray distribution.

It is likely that many subduction zone tomography models obtained through the isotropic approximation are contaminated to some degree by anisotropy-related artifacts. Our results suggest that some of these artifacts may be attractive targets for (mis)interpretation, and thus we would urge caution when interpreting isotropic velocity models of subduction zones where anisotropy is known to be of an important magnitude.

The methods currently in use to measure the propensity of tomography models to artifacts (synthetic tests, bootstrapping) are probably inadequate. Since they do not account for the effect of the anisotropy that is known to exist, they provide an overly optimistic view of the accuracy of our models and may provide a false sense of confidence on the results.

We have shown that incorporating the anisotropy field as an a priori constraint on the tomography inversions can be an effective way to reduce the occurrence of artifacts in the models. While the anisotropy field will never be exactly known, we have shown that useful results can be derived even from coarse approximations thereof, and that the model norm and data misfit can be used to determine if a particular anisotropy field is an improvement over the standard zero-anisotropy approximation. Approximate anisotropy fields may be derived from geodynamic modeling and constrained by seismic observables, including shear-wave splitting measurements. We propose that incorporating physically based estimates of the anisotropy distribution, perhaps coupled with targeted inversions for a reduced set of parameters describing the anisotropy, can be a viable way forward for addressing this problem without having to invert for anisotropy in every node. Future research will test the applicability of this paradigm to field data.

Acknowledgments

All model results, as well as event locations, isotropic, and anisotropic delay times for all cases are archived by the authors and are available upon request (mbezada@umn.edu). The data and model files are archived at the University of Minnesota-Twin Cities. Input from three anonymous reviewers on a preliminary version of the manuscript helped strengthen this paper considerably. This research was funded by NSF grant EAR-1520695.

References

Alpert, L. A., M. S. Miller, T. W. Becker, and A. A. Allam (2013), Structure beneath the Alboran from geodynamic flow models and seismic anisotropy, *J. Geophys. Res. Solid Earth*, *118*, 4265–4277, doi:10.1002/jgrb.50309.

Baccheschi, P., L. Margheriti, and M. S. Steckler (2007), Seismic anisotropy reveals focused mantle flow around the Calabrian slab (Southern Italy), *Geophys. Res. Lett.*, *34*, L05302, doi:10.1029/2006GL028899.

Becker, T. W., V. Schulte-Pelkum, D. K. Blackman, J. B. Kellogg, and R. J. O'Connell (2006a), Mantle flow under the western United States from shear wave splitting, *Earth Planet. Sci. Lett.*, *247*(3–4), 235–251, doi:10.1016/j.epsl.2006.05.010.

Becker, T. W., S. Chevrot, V. Schulte-Pelkum, and D. K. Blackman (2006b), Statistical properties of seismic anisotropy predicted by upper mantle geodynamic models, *J. Geophys. Res.*, *111*, B08309, doi:10.1029/2005JB004095.

Bezada, M. J., A. Levander, and B. Schmandt (2010), Subduction in the southern Caribbean: Images from finite-frequency P wave tomography, *J. Geophys. Res.*, *115*, B12333, doi:10.1029/2010JB007682.

Bezada, M. J., E. D. Humphreys, D. R. Toomey, M. Harnafi, J. M. Dávila, and J. Gallart (2013), Evidence for slab rollback in westernmost Mediterranean from improved upper mantle imaging, *Earth Planet. Sci. Lett.*, *368*, 51–60, doi:10.1016/j.epsl.2013.02.024.

Bijwaard, H., and W. Spakman (1999), Tomographic evidence for a narrow whole mantle plume below Iceland, *Earth Planet. Sci. Lett.*, *166*(3–4), 121–126, doi:10.1016/S0012-821X(99)00004-7.

Blackman, D. K., and J.-M. Kendall (1997), Sensitivity of teleseismic body waves to mineral texture and melt in the mantle beneath a mid-ocean ridge, *Philos. Trans. R. Soc. London A*, *355*(1723), 217–231, doi:10.1098/rsta.1997.0007.

Blackman, D. K., J.-M. Kendall, P. R. Dawson, H.-R. Wenk, D. Boyce, and J. P. Morgan (1996), Teleseismic imaging of subaxial flow at mid-ocean ridges: Traveltime effects of anisotropic mineral texture in the mantle, *Geophys. J. Int.*, *127*(2), 415–426, doi:10.1111/j.1365-246X.1996.tb04730.x.

Bodmer, M., D. R. Toomey, E. E. Hooft, J. Nábělek, and J. Braunmiller (2015), Seismic anisotropy beneath the Juan de Fuca plate system: Evidence for heterogeneous mantle flow, *Geology*, *43*(12), 1095–1098, doi:10.1130/G37181.1.

Cammarano, F., S. Goes, P. Vacher, and D. Giardini (2003), Inferring upper-mantle temperatures from seismic velocities, *Phys. Earth Planet. Inter.*, *138*(3–4), 197–222, doi:10.1016/S0031-9201(03)00156-0.

Conder, J. A., and D. A. Wiens (2006), Seismic structure beneath the Tonga arc and Lau back-arc basin determined from joint Vp, Vp/Vs tomography, *Geochem. Geophys. Geosyst.*, *7*, Q03018, doi:10.1029/2005GC001113.

Diaz, J., J. Gallart, A. Villasenor, F. Mancilla, A. Pazos, D. Cordoba, J. A. Pulgar, P. Ibarra, and M. Harnafi (2010), Mantle dynamics beneath the Gibraltar Arc (western Mediterranean) from shear-wave splitting measurements on a dense seismic array, *Geophys. Res. Lett.*, *37*, L18304, doi:10.1029/2010GL044201.

Dijkstra, E. W. (1959), A note on two problems in connexion with graphs, *Numer. Math.*, *1*(1), 269–271, doi:10.1007/BF01386390.

Eakin, C. M., M. Obrebski, R. M. Allen, D. C. Boyarko, M. R. Brudzinski, and R. Porritt (2010), Seismic anisotropy beneath Cascadia and the Mendocino triple junction: Interaction of the subducting slab with mantle flow, *Earth Planet. Sci. Lett.*, *297*(3–4), 627–632, doi:10.1016/j.epsl.2010.07.015.

Eberhart-Phillips, D., and C. M. Henderson (2004), Including anisotropy in 3-D velocity inversion and application to Marlborough, New Zealand, *Geophys. J. Int.*, *156*(2), 237–254, doi:10.1111/j.1365-246X.2003.02044.x.

Eberhart-Phillips, D., and M. Reyners (2009), Three-dimensional distribution of seismic anisotropy in the Hikurangi subduction zone beneath the central North Island, New Zealand, *J. Geophys. Res.*, *114*, B06301, doi:10.1029/2008JB005947.

Faccenda, M. (2014), Mid mantle seismic anisotropy around subduction zones, *Phys. Earth Planet. Inter.*, *227*, 1–19, doi:10.1016/j.pepi.2013.11.015.

Faccenda, M., and F. A. Capitanio (2012), Development of mantle seismic anisotropy during subduction-induced 3-D flow, *Geophys. Res. Lett.*, *39*, L11305, doi:10.1029/2012GL051988.
Faccenda, M., and F. A. Capitanio (2013), Seismic anisotropy around subduction zones: Insights from three-dimensional modeling of upper mantle deformation and SKS splitting calculations, *Geochem. Geophys. Geosyst.*, *14*, 243–262, doi:10.1002/ggge.20055.
Faccenna, C., and T. W. Becker (2010), Shaping mobile belts by small-scale convection, *Nature*, *465*(7298), 602–605, doi:10.1038/nature09064.
Goes, S., and S. van der Lee (2002), Thermal structure of the North American uppermost mantle inferred from seismic tomography, *J. Geophys. Res.*, *107*(B3), 2050, doi:10.1029/2000JB000049.
Goes, S., R. Govers, and P. Vacher (2000), Shallow mantle temperatures under Europe from P and S wave tomography, *J. Geophys. Res.*, *105*(B5), 11,153–11,169.
Grésillaud, A., and M. Cara (1996), Anisotropy and P-wave tomography: A new approach for inverting teleseismic data from a dense array of stations, *Geophys. J. Int.*, *126*(1), 77–91, doi:10.1111/j.1365-246X.1996.tb05268.x.
Hammond, W. C., and E. D. Humphreys (2000), Upper mantle seismic wave velocity: Effects of realistic partial melt geometries, *J. Geophys. Res.*, *105*(B5), 10,975–10,986, doi:10.1029/2000JB900041.
Hammond, W. C., and D. R. Toomey (2003), Seismic velocity anisotropy and heterogeneity beneath the Mantle Electromagnetic and Tomography Experiment (MELT) region of the East Pacific Rise from analysis of P and S body waves, *J. Geophys. Res.*, *108*(B4), 2176, doi:10.1029/2002JB001789.
Huang, Z., D. Zhao, and X. Liu (2015), On the trade-off between seismic anisotropy and heterogeneity: Numerical simulations and application to Northeast Japan, *J. Geophys. Res. Solid Earth*, *120*, 3255–3277, doi:10.1002/2014JB011784.
Husen, S., E. Kissling, and E. R. Flueh (2000), Local earthquake tomography of shallow subduction in north Chile: A combined onshore and offshore study, *J. Geophys. Res.*, *105*(B12), 28,183–28,198, doi:10.1029/2000JB900229.
Ishise, M., and H. Oda (2005), Three-dimensional structure of P-wave anisotropy beneath the Tohoku district, northeast Japan, *J. Geophys. Res.*, *110*, B07304, doi:10.1029/2004JB003599.
Jackson, I., and U. H. Faul (2010), Grainsize-sensitive viscoelastic relaxation in olivine: Towards a robust laboratory-based model for seismological application, *Phys. Earth Planet. Inter.*, *183*(1–2), 151–163, doi:10.1016/j.pepi.2010.09.005.
Kaminski, É., N. M. Ribe, and J. T. Browaeys (2004), D-Rex, a program for calculation of seismic anisotropy due to crystal lattice preferred orientation in the convective upper mantle, *Geophys. J. Int.*, *158*(2), 744–752, doi:10.1111/j.1365-246X.2004.02308.x.
Karato, S., and H. Jung (1998), Water, partial melting and the origin of the seismic low velocity and high attenuation zone in the upper mantle, *Earth Planet. Sci. Lett.*, *157*(3–4), 193–207, doi:10.1016/S0012-821X(98)00034-X.
Karato, S., H. Jung, I. Katayama, and P. Skemer (2008), Geodynamic significance of seismic anisotropy of the upper mantle: New insights from laboratory studies, *Annu. Rev. Earth Planet. Sci.*, *36*(1), 59–95, doi:10.1146/annurev.earth.36.031207.124120.
Kendall, J.-M. (1994), Teleseismic arrivals at a mid-ocean ridge: Effects of mantle melt and anisotropy, *Geophys. Res. Lett.*, *21*(4), 301–304, doi:10.1029/93GL02791.
Koulakov, I., A. Jakovlev, and B. G. Luehr (2009), Anisotropic structure beneath central Java from local earthquake tomography, *Geochem. Geophys. Geosyst.*, *10*, Q02011, doi:10.1029/2008GC002109.
Levander, A., et al. (2006), Evolution of the southern Caribbean Plate boundary, *Eos Trans. AGU*, *87*(9), 97–100.
Liu, K. H., A. Elsheikh, A. Lemnifi, U. Purevsuren, M. Ray, H. Refayee, B. B. Yang, Y. Yu, and S. S. Gao (2014), A uniform database of teleseismic shear wave splitting measurements for the western and central United States, *Geochem. Geophys. Geosyst.*, *15*, 2075–2085, doi:10.1002/2014GC005267.
Lloyd, S. M., and S. van der Lee (2008), Influence of observed mantle anisotropy on isotropic tomographic models, *Geochem. Geophys. Geosyst.*, *9*, Q07007, doi:10.1029/2008GC001997.
Long, M. D. (2013), Constraints on subduction geodynamics from seismic anisotropy, *Rev. Geophys.*, *51*, 76–112, doi:10.1002/rog.20008.
Long, M. D., and P. G. Silver (2008), The subduction zone flow field from seismic anisotropy: A global view, *Science*, *319*(5861), 315–318, doi:10.1126/science.1150809.
Long, M. D., and P. G. Silver (2009), Shear wave splitting and mantle anisotropy: Measurements, interpretations, and new directions, *Surv. Geophys.*, *30*(4–5), 407–461, doi:10.1007/s10712-009-9075-1.
Mainprice, D. (1997), Modelling the anisotropic seismic properties of partially molten rocks found at mid-ocean ridges, *Tectonophysics*, *279*(1–4), 161–179, doi:10.1016/S0040-1951(97)00122-4.
Mainprice, D. (2007), 2.16: Seismic anisotropy of the deep earth from a mineral and rock physics perspective, in *Treatise on Geophysics*, edited by G. Schubert, pp. 437–491, Elsevier, Amsterdam.
Miller, M. S., A. A. Allam, T. W. Becker, J. F. Di Leo, and J. Wookey (2013), Constraints on the tectonic evolution of the westernmost Mediterranean and northwestern Africa from shear wave splitting analysis, *Earth Planet. Sci. Lett.*, *375*, 234–243, doi:10.1016/j.epsl.2013.05.036.
Moser, T. (1991), Shortest path calculation of seismic rays, *Geophysics*, *56*(1), 59–67, doi:10.1190/1.1442958.
Olive, J.-A., F. Pearce, S. Rondenay, and M. D. Behn (2014), Pronounced zonation of seismic anisotropy in the Western Hellenic subduction zone and its geodynamic significance, *Earth Planet. Sci. Lett.*, *391*, 100–109, doi:10.1016/j.epsl.2014.01.029.
Paulatto, M., C. Annen, T. J. Henstock, E. Kiddle, T. A. Minshull, R. S. J. Sparks, and B. Voight (2012), Magma chamber properties from integrated seismic tomography and thermal modeling at Montserrat, *Geochem. Geophys. Geosyst.*, *13*, Q01014, doi:10.1029/2011GC003892.
Russo, R. M., and P. G. Silver (1994), Trench-parallel flow beneath the Nazca plate from seismic anisotropy, *Science*, *263*(5150), 1105–1111, doi:10.1126/science.263.5150.1105.
Schmandt, B., and E. Humphreys (2010), Seismic heterogeneity and small-scale convection in the southern California upper mantle, *Geochem. Geophys. Geosyst.*, *11*, Q05004, doi:10.1029/2010GC003042.
Schurr, B., A. Rietbrock, G. Asch, R. Kind, and O. Oncken (2006), Evidence for lithospheric detachment in the central Andes from local earthquake tomography, *Tectonophysics*, *415*(1–4), 203–223, doi:10.1016/j.tecto.2005.12.007.
Sieminski, A., Q. Liu, J. Trampert, and J. Tromp (2007), Finite-frequency sensitivity of body waves to anisotropy based upon adjoint methods, *Geophys. J. Int.*, *171*(1), 368–389, doi:10.1111/j.1365-246X.2007.03528.x.
Sobolev, S. V., H. Zeyen, M. Granet, U. Achauer, C. Bauer, F. Werling, R. Altherr, and K. Fuchs (1997), Upper mantle temperatures and lithosphere-asthenosphere system beneath the French Massif Central constrained by seismic, gravity, petrologic and thermal observations, *Tectonophysics*, *275*(1–3), 143–164, doi:10.1016/S0040-1951(97)00019-X.
Sobolev, S. V., A. Grésillaud, and M. Cara (1999), How robust is isotropic delay time tomography for anisotropic mantle?, *Geophys. Res. Lett.*, *26*(4), 509–512, doi:10.1029/1998GL900206.
Takei, Y. (2002), Effect of pore geometry on VP/VS: From equilibrium geometry to crack, *J. Geophys. Res.*, *107*(B2), 2043, doi:10.1029/2001JB000522.

Tian, Y., and D. Zhao (2012), Seismic anisotropy and heterogeneity in the Alaska subduction zone, *Geophys. J. Int.*, *190*(1), 629–649, doi: 10.1111/j.1365-246X.2012.05512.x.

Toomey, D., S. Solomon, and G. Purdy (1994), Tomographic imaging of the shallow crustal structure of the East Pacific Rise at 9-Degrees-30'n, *J. Geophys. Res.*, *99*(B12), 24,135–24,157, doi:10.1029/94JB01942.

Toomey, D. R., W. S. D. Wilcock, S. C. Solomon, W. C. Hammond, and J. A. Orcutt (1998), Mantle seismic structure beneath the MELT region of the East Pacific rise from p and s wave tomography, *Science*, *280*(5367), 1224–1227, doi:10.1126/science.280.5367.1224.

Villagómez, D. R., D. R. Toomey, D. J. Geist, E. E. E. Hooft, and S. C. Solomon (2014), Mantle flow and multistage melting beneath the Galapagos hotspot revealed by seismic imaging, *Nat. Geosci.*, *7*(2), 151–156, doi:10.1038/ngeo2062.

Wang, J., and D. Zhao (2013), P-wave tomography for 3-D radial and azimuthal anisotropy of Tohoku and Kyushu subduction zones, *Geophys. J. Int.*, *193*(3), 1166–1181, doi:10.1093/gji/ggt086.

Wiens, D. A., J. A. Conder, and U. H. Faul (2008), The seismic structure and dynamics of the mantle wedge, *Annu. Rev. Earth Planet. Sci.*, *36*(1), 421–455, doi:10.1146/annurev.earth.33.092203.122633.

Wolfe, C. J., S. C. Solomon, G. Laske, J. A. Collins, R. S. Detrick, J. A. Orcutt, D. Bercovici, and E. H. Hauri (2009), Mantle shear-wave velocity structure beneath the hawaiian hot spot, *Science*, *326*(5958), 1388–1390, doi:10.1126/science.1180165.

Wu, H., and J. M. Lees (1999), Cartesian parametrization of anisotropic traveltime tomography, *Geophys. J. Int.*, *137*(1), 64–80, doi:10.1046/j.1365-246x.1999.00778.x.

Zhao, D., A. Hasegawa, and S. Horiuchi (1992), Tomographic imaging of P-wave and S-wave velocity structure beneath Northeastern Japan, *J. Geophys. Res.*, *97*(B13), 19,909–19,928, doi:10.1029/92JB00603.